molecules

MDPI

Article

The Role of Intraligand Charge Transfer Processes in Iridium(III) Complexes with Morpholine-Decorated 4′-Phenyl-2,2′:6′,2″-terpyridine

Joanna Palion-Gazda *, Aleksandra Kwiecień, Katarzyna Choroba, Mateusz Penkala, Anna Kryczka and Barbara Machura *

Institute of Chemistry, University of Silesia, 9 Szkolna Str., 40-006 Katowice, Poland; aleksandra.a.kwiecien@us.edu.pl (A.K.); katarzyna.choroba@us.edu.pl (K.C.); mateusz.penkala@us.edu.pl (M.P.); akryczka1@us.edu.pl (A.K.)

* Correspondence: joanna.palion-gazda@us.edu.pl (J.P.-G.); barbara.machura@us.edu.pl (B.M.)

Abstract: To investigate the impact of the electron-donating morpholinyl (morph) group on the ground- and excited-state properties of two different types of Ir(III) complexes, $[IrCl_3(R\text{-}C_6H_4\text{-terpy-}\kappa^3N)]$ and $[Ir(R\text{-}C_6H_4\text{-terpy-}\kappa^3N)_2](PF_6)_3$, the compounds $[IrCl_3(morph\text{-}C_6H_4\text{-terpy-}\kappa^3N)]$ (**1A**), $4[Ir(morph\text{-}C_6H_4\text{-terpy-}\kappa^3N)_2](PF_6)_3$ (**2A**), $[IrCl_3(Ph\text{-terpy-}\kappa^3N)]$ (**1B**) and $[Ir(Ph\text{-terpy-}\kappa^3N)_2](PF_6)_3$ (**2B**) were obtained. Their photophysical properties were comprehensively investigated with the aid of static and time-resolved spectroscopic methods accompanied by theoretical DFT/TD-DFT calculations. In the case of bis-terpyridyl iridium(III) complexes, the attachment of the morpholinyl group induced dramatic changes in the absorption and emission characteristics, manifested by the appearance of a new, very strong visible absorption tailing up to 600 nm, and a significant bathochromic shift in the emission of **2A** relative to the model chromophore. The emission features of **2A** and **2B** were found to originate from the triplet excited states of different natures: intraligand charge transfer (^{3}ILCT) for **2A** and intraligand with a small admixture of metal-to-ligand charge transfer (^{3}IL–^{3}MLCT) for **2B**. The optical properties of the mono-terpyridyl iridium(III) complexes were less significantly impacted by the morpholinyl substituent. Based on UV–Vis absorption spectra, emission wavelengths and lifetimes in different environments, transient absorption studies, and theoretical calculations, it was demonstrated that the visible absorption and emission features of **1A** are governed by singlet and triplet excited states of a mixed MLLCT-ILCT nature, with a dominant contribution of the first component, that is, metal-ligand-to-ligand charge transfer (MLLCT). The involvement of ILCT transitions was reflected by an enhancement of the molar extinction coefficients of the absorption bands of **1A** in the range of 350–550 nm, and a small red shift in its emission relative to the model chromophore.

Keywords: iridium(III) complexes; 4′-subsituted 2,2′:6′,2″-terpyridines; absorption and emission characteristics; intraligand and metal-to-ligand charge-transfer processes

check for updates

Citation: Palion-Gazda, J.; Kwiecień, A.; Choroba, K.; Penkala, M.; Kryczka, A.; Machura, B. The Role of Intraligand Charge Transfer Processes in Iridium(III) Complexes with Morpholine-Decorated 4′-Phenyl-2,2′:6′,2″-terpyridine. *Molecules* **2024**, *29*, 3074. https://doi.org/10.3390/molecules29133074

Academic Editor: Conor Long

Received: 3 June 2024
Revised: 24 June 2024
Accepted: 25 June 2024
Published: 27 June 2024

Copyright: © 2024 by the authors. Licensee MDPI, Basel, Switzerland. This article is an open access article distributed under the terms and conditions of the Creative Commons Attribution (CC BY) license (https://creativecommons.org/licenses/by/4.0/).

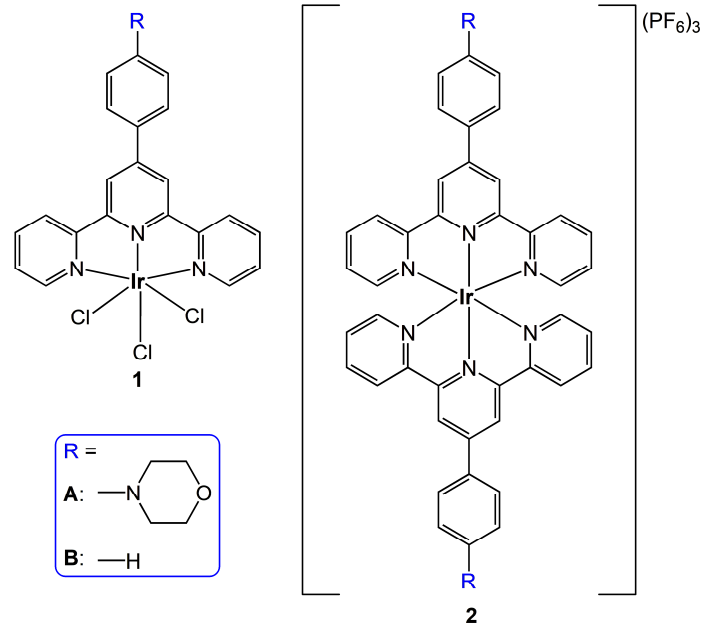
1. Introduction

4′-subsituted 2,2′:6′,2″-terpyridines (R-terpys) are among the most important building blocks in coordination chemistry [1–6]. When combined with numerous transition metal ions, they provide opportunities to obtain mono- and polynuclear coordination compounds suitable for applications in optoelectronics [7–12], photocatalysis [1,13–18], chemotherapy, and photodynamic therapy [19–27]. Thanks to the highly convenient Krönhke methodology [28], the functional properties of R-terpys and their transition metal complexes can be widely tuned, allowing for further progress in the improvement of phosphorescent materials and potent chemotherapeutic drugs.

Recently, significant effort has been dedicated to understanding the impact of substituents attached via aryl linkers to the central pyridine ring of the terpy backbone. The

crucial role of the remote substituent of R-C_6H_4-terpys in controlling the ground- and excited-state properties of [ReCl(CO)$_3$(R-C_6H_4-terpy-κ^2N)] was confirmed by Fernández-Terán [14,29] and our research groups [30–36]. The optical properties of [ReCl(CO)$_3$(R-C_6H_4-terpy-κ^2N)] were found to systematically vary with increasing electron-donating abilities of the appended groups (–CN < –CF_3 < –Br < –H < –OMe), as manifested by a hypsochromic shift of the metal-ligand-to-ligand charge transfer (^{1}MLLCT) absorption and ^{3}MLLCT emission bands, increased ^{3}MLLCT lifetimes, and $\Delta G_{S\text{-}T}$ from –CN to –OMe. The introduction of the stronger electron-donating group –NMe_2 resulted in a switch of the excited state from ^{3}MLLCT (with –CN, –CF_3, –Br, and –OMe groups) to intraligand charge transfer ^{3}ILCT (–NMe_2), which was reflected in a dramatically enhanced visible light absorption band, prolonged excited-state lifetime in solution, red shift of the emission upon cooling, and improved photocatalytic properties of [ReCl(CO)$_3$(Me_2N-C_6H_4-terpy-κ^2N)] in hydrogen evaluation experiments [14]. As demonstrated by our research group [36], the photoinduced processes in [ReCl(CO)$_3$(R-C_6H_4-terpy-κ^2N)] with remote electron-donating N-methyl-piperazinyl and (2-cyanoethyl)methylamine groups were additionally affected by the polarity environment. Increased solvent polarity favored the population of the ^{3}ILCT excited state, leading to much more extended triplet excited-state lifetimes in polar solvents. Conversely to those of [ReCl(CO)$_3$(R-C_6H_4-terpy-κ^2N)], the optical properties of the Re(I) carbonyl complexes with meridonally co-ordinated 4′-subsituted 2,2′:6′,2″-terpyridines [ReCl(CO)$_2$(Me_2N-C_6H_4-terpy-κ^3N)] were governed by MLLCT excited states, independent of the electron-donating abilities of the pendant group of R-C_6H_4-terpy. The more electron-rich {Re(CO)$_2$}$^+$ moiety in [ReX(CO)$_2$(R-C_6H_4-terpy-κ^3N)] systems was found to hinder access to ILCT excited states [14].

In the current work, we investigated the effect of the electron-donating morpholinyl (morph) group on ground- and excited-state properties of two different types of Ir(III) complexes: [$IrCl_3$(R-C_6H_4-terpy-κ^3N)] and [Ir(R-C_6H_4-terpy-κ^3N)$_2$](PF_6)$_3$ (Scheme 1).



Scheme 1. Chemical structures of investigated Ir(III) compounds.

The photophysical properties of [$IrCl_3$(morph-C_6H_4-terpy-κ^3N)] (**1A**) and [Ir(morph-C_6H_4-terpy-κ^3N)$_2$](PF_6)$_3$ (**2A**) were comprehensively explored using static and time-resolved spectroscopic methods, accompanied by theoretical DFT/TD-DFT calculations, and analyzed in comparison to the photobehavior of the corresponding parent chromophores [$IrCl_3$(Ph-terpy-κ^3N)] (**1B**) and [Ir(Ph-terpy-κ^3N)$_2$](PF_6)$_3$ (**2B**), which was partially dis-

cussed in [37,38]. We demonstrated that the morpholinyl remote group has a significantly larger impact on the photophysical behavior of the bis-terpyridyl Ir(III) complex.

2. Results and Discussion

The complexes [$IrCl_3$(R-C_6H_4-terpy-κ^3N)] (**1A** and **1B**) and [Ir(R-C_6H_4-terpy-κ^3N)$_2$]$(PF_6)_3$ (**2A** and **2B**) were prepared using conventional synthetic procedures [39–41]. Specifically, the iridium(III) chloride salt was heated with one equivalent of the appropriate R-C_6H_4-terpy ligand in methoxyethanol to synthesize **1A** and **1B**. The corresponding [$IrCl_3$(R-C_6H_4-terpy-κ^3N)] complex was then reacted with a slight excess of R-C_6H_4-terpy in ethylene glycol to obtain **2A** and **2B**. The identity and composition of **1**–**2** was confirmed by elemental analysis, ^{1}H and ^{13}C NMR spectroscopies (Figures 1 and S1–S4), and the FT-IR technique (Figure S5).

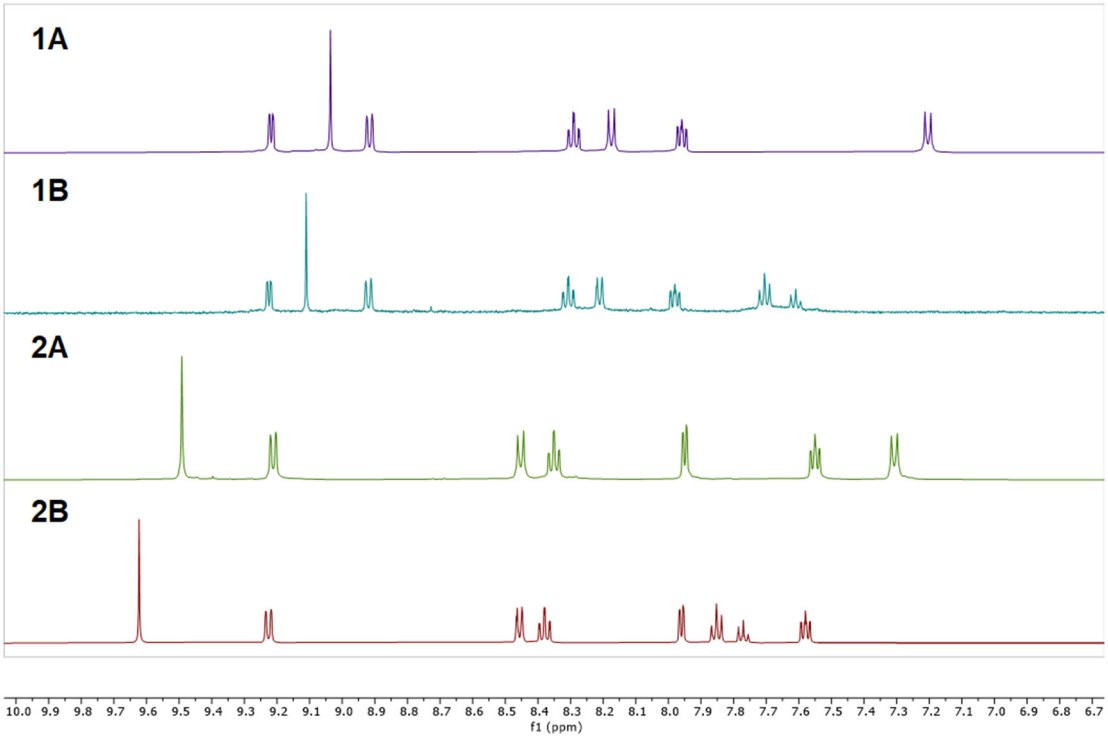


Figure 1. Proton signals of Ir(III) complexes.

As demonstrated in Figure 1, the proton signals of the central pyridine ring in the terpyridine backbone (represented by the singlet) were noticeably shifted upfield in the morpholinyl-substituted Ir(III) systems, indicating that the appended electron-donating morpholine group affects the electron density in the distal part of the ligand molecule. The difference in chemical shifts, from 9.11 ppm for **1B** to 9.04 ppm for **1A** and from 9.62 ppm for **2B** to 9.49 for **2A**, shows that this effect was stronger for the cationic Ir(III) complexes.

The FT-IR spectra of all the investigated Ir(III) complexes displayed characteristic bands in the region 1615–1525 cm^{-1}, attributable to $\nu(C{=}N)_{terpy}$ and $\nu(C{=}C)_{terpy}$ stretches. The intense bands occurring at ~840 cm^{-1} and ~555 cm^{-1} in the FT-IR spectra of **2A** and **2B** are indicative of PF_6^- ions (Figure S5) [42].

Additionally, the molecular structures of **1A**, **1B**, and **2B** were unambiguously determined by X-ray analysis. The full structural data of these systems are provided in the Supplementary Materials (Tables S1–S4 and Figure S6). Perspective views of the molecular structures of **1A**, **1B**, and **2B**, with atom numbering, are depicted in Figure 2, while the most relevant bond lengths and angles are summarized in Table 1.

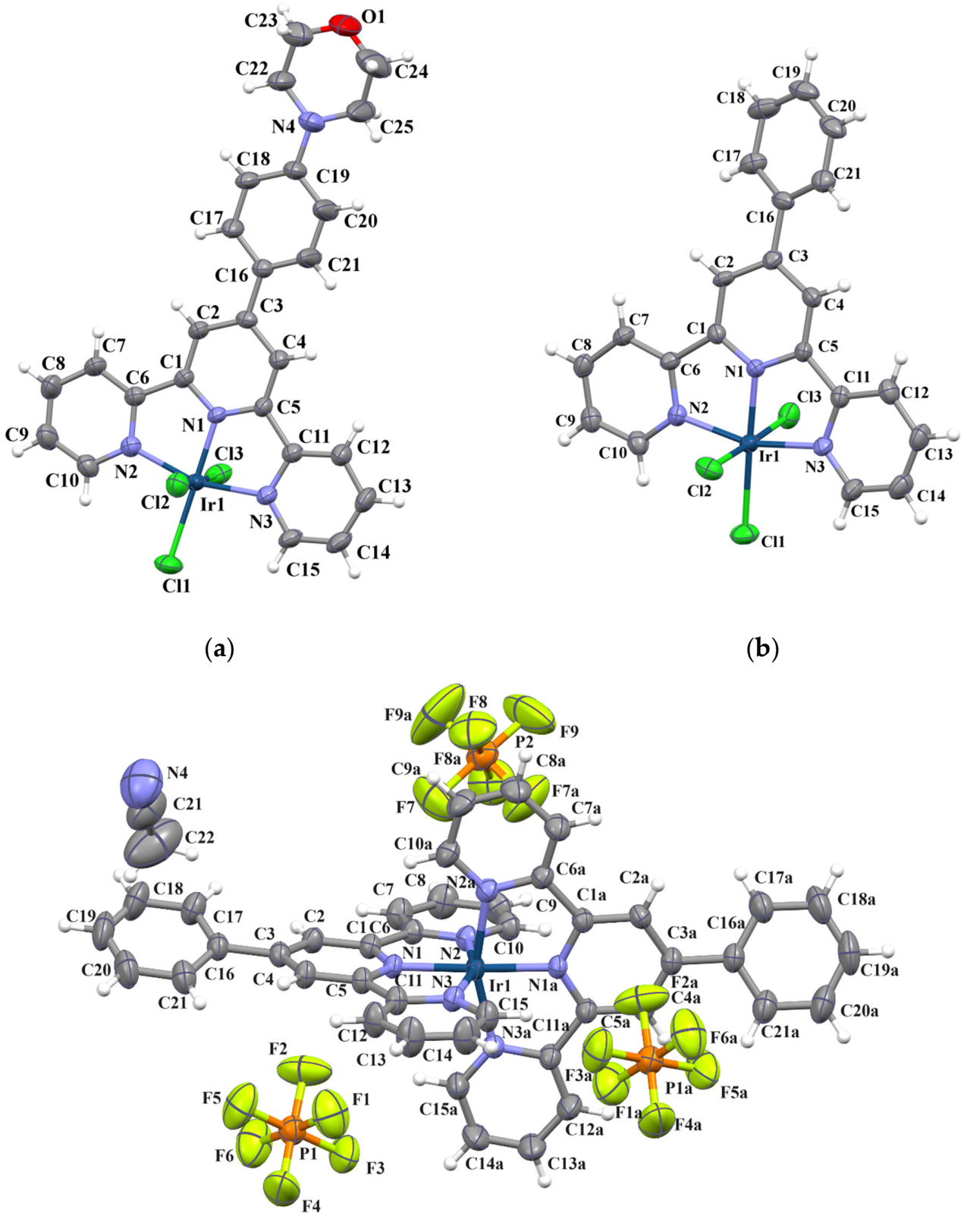


Figure 2. Molecular structures of **1A** (**a**), **1B** (**b**), and **2B** (**c**), with the atom numbering and thermal ellipsoids set at 50% probability for non-hydrogen atoms. (Symmetry code for **2B**: (a) = $2 - x, y, 3/2 - z$).

Table 1. Experimental bond lengths [Å] and angles [°] for **1A**, **1B**, and **2B**.

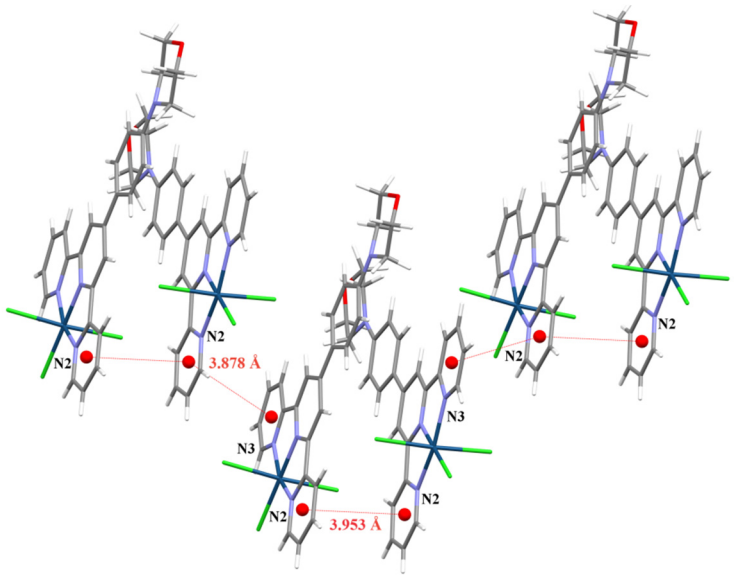
	1A	**1B**	**2B**
Bond length [Å]			
Ir(1)–Cl(1)	2.372(1)	2.375(2)	
Ir(1)–Cl(2)	2.361(2)	2.347(2)	
Ir(1)–Cl(3)	2.363(1)	2.362(2)	
Ir(1)–N(1)	1.935(4)	1.938(5)	1.974(3)
Ir(1)–N(2)	2.046(4)	2.040(5)	2.051(3)
Ir(1)–N(3)	2.028(4)	2.045(5)	2.056(3)
Bond angle [°]			
Cl(1)–Ir(1)–Cl(2)	92.55(60)	90.03(60)	
Cl(1)–Ir(1)–Cl(3)	91.40(60)	91.29 (60)	
Cl(2)–Ir(1)–Cl(3)	175.67(50)	178.43(60)	
Cl(1)–Ir(1)–N(1)	179.39(13)	177.15(14)	
Cl(1)–Ir(1)–N(2)	98.69(12)	99.80(15)	
Cl(1)–Ir(1)–N(3)	99.39(12)	99.00(14)	
Cl(2)–Ir(1)–N(1)	86.93(12)	92.80(14)	
Cl(2)–Ir(1)–N(2)	91.46(12)	90.56(14)	
Cl(2)–Ir(1)–N(3)	87.92(12)	88.66(15)	
Cl(3)–Ir(1)–N(1)	89.13(12)	85.88(14)	
Cl(3)–Ir(1)–N(2)	89.69(12)	88.37(14)	
Cl(3)–Ir(1)–N(3)	89.70(13)	91.98(15)	
N(1)–Ir(1)–N(1a)			177.47(16)
N(1)–Ir(1)–N(2)	80.99(16)	80.53(19)	79.82 (11)
N(1)–Ir(1)–N(2a)			98.43(11)
N(1)–Ir(1)–N(3)	80.93(16)	80.73(19)	79.90(11)
N(1)–Ir(1)–N(3a)			101.88(11)
N(2)–Ir(1)–N(2a)			93.62(17)
N(2)–Ir(1)–N(3)	161.92(16)	161.18(19)	159.70(11)
N(2)–Ir(1)–N(3a)			90.27(12)
N(3)–Ir(1)–N(3a)			92.97(17)

In all reported complexes, the Ir(III) ion was located in a distorted octahedral environment. The coordination sphere of **1A** and **1B** was defined by three chloride ions and three nitrogen atoms of the tridendate-coordinated R-C_6H_4-terpy (κ^3N) ligand. Due to the geometrical constraints imposed by the planar terpy framework, both nitrogen and chlorine donor atoms adopted meridional arrangements. The crystal structure of **2B** consisted of the complex cations $[Ir(Ph\text{-}terpy\text{-}\kappa^3N)_2]^{3+}$, PF_6^- counteranions in a 1:3 molar ratio, and solvent (MeCN) molecules. The metal center of $[Ir(Ph\text{-}terpy\text{-}\kappa^3N)_2]^{3+}$ was octahedrally surrounded by six nitrogen atoms from two Ph-terpy-κ^3N ligands, coordinated in a *mer*-fashion.

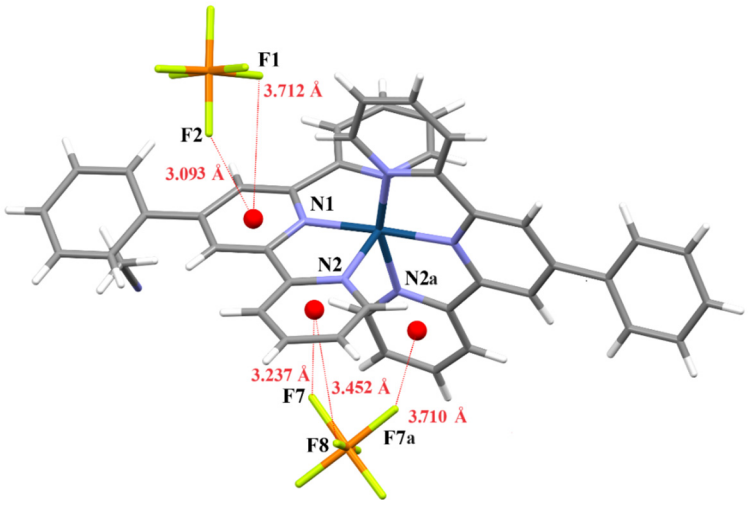
Typical of the terpy-κ^3N coordination mode [43], the Ir–N bond lengths involving peripheral pyridine rings in structures **1A**, **1B**, and **2B** were longer than the Ir–$N_{central\ pyridine}$ distances (Table 1). The shortening of the Ir–$N_{central\ pyridine}$ bond length was rationalized by a more efficient overlap of the t_{2g} metal orbitals with the π^* orbitals of the central pyridine relative to the peripheral pyridyl groups. Consequently, the chloride ligand *trans*-located to the central pyridine ring of R-C_6H_4-terpy in molecules **1A** and **1B** exhibited an elongated bond distance in relation to the other Ir–Cl ones (Table 1).

In all the studied Ir(III) complexes, a considerable angular distortion from the octahedral geometry was reflected in the N–Ir–N bite angles due to the formation of five-membered metallocycles upon the chelating coordination of R-C_6H_4-terpy. The N–Ir–N bite angles varied from 79.84(12) to 80.99(16)° (Table 1). The terpy framework in structures **1A**, **1B**, and **2B** showed good planarity, with the dihedral angles between the mean planes of the central pyridine and terminal aromatic rings ranging from 1.26° to 7.92°. The plane of the phenyl ring of **1A** maintained near co-planarity (1.92°) with the central pyridine plane, while in the model compounds, it was inclined to the central pyridine by 20.48° in **1B**, and 23.46° in **2B**.

The arrangement of molecules $[IrCl_3(R\text{-}C_6H_4\text{-terpy-}\kappa^3N)]$ in the crystal structures of **1A** and **1B** was governed by π•••π stacking interactions and weak hydrogen bonds (C–H•••Cl and C–H•••O). The crystal packing analysis of **2B** revealed interactions between the cations $[Ir(Ph\text{-terpy-}\kappa^3N)_2]^{3+}$ and anions PF_6^-, facilitated by weak hydrogen bonds (C–H•••F) and P–F•••π contacts (Figure 3 and Tables S2 and S4). The shortest Ir•••F distances were 5.542 Å and 5.940 Å.



(**a**)



(**b**)

Figure 3. View of the supramolecular chain of $[IrCl_3(morph\text{-}C_6H_4\text{-terpy-}\kappa^3N)]_n$ resulting from weak π•••π interactions indicated by red dashed line (**a**); C–H•••F and P–F•••π contacts between the cations $[Ir(Ph\text{-terpy-}\kappa^3N)_2]^{3+}$ and anions PF_6^- in the structure **2B** (**b**) (see also Figure S6 and Tables S2–S4).

3. Ground-State Molecular Orbitals

To better understand the impact of the electron-donating morpholinyl group on the photophysical behavior of the $[IrCl_3(R\text{-}C_6H_4\text{-terpy-}\kappa^3N)]$ (**1A**, **1B**) and $[Ir(R\text{-}C_6H_4\text{-terpy-}\kappa^3N)_2](PF_6)_3$ (**2A**, **2B**) systems, the energies and electron distributions of the highest occupied (HOMO) and lowest unoccupied (LUMO) molecular orbitals are briefly presented

prior to the discussion of the optical properties of **1A**–**2A** and **1B**–**2B**. DFT calculations were performed using Gaussian-16 software [44] at the TD-DFT/PCM/PBE0/SDD/def2-TZVP level [45] (Figure 4, Tables S5–S7, Figure S7).

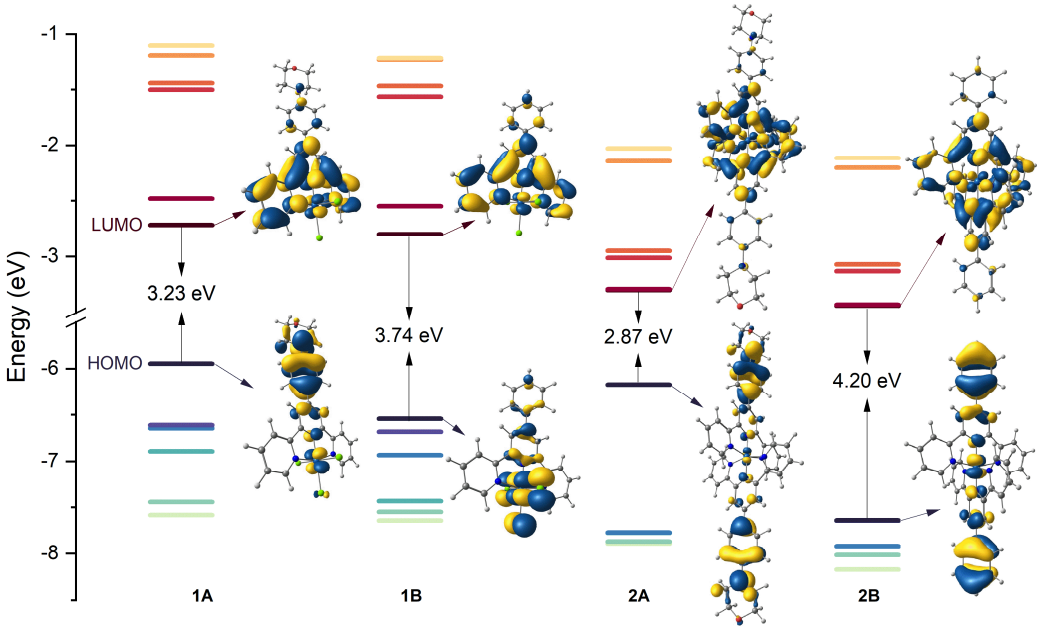


Figure 4. The partial molecular orbital energy level diagram with the plots of electron density distributions in the HOMO and LUMO of **1A**–**2A** and **1B**–**2B**.

As shown in Figure 4, the attachment of the morpholinyl group to Ph-terpy led to the destabilization of both the HOMO and LUMO orbitals, with more pronounced energy variations in the case of the HOMO level. In the pairs **1A**–**1B** and **2A**–**2B**, the HOMO energy increased by ~0.60 eV and ~1.47 eV upon going from the unsubstituted to the morpholinyl-decorated system, respectively. The destabilization of the LUMO level due to the morpholine incorporation was ~0.08 eV and ~0.14 eV for pairs **1A**–**1B** and **2A**–**2B**. Consequently, the Ir(III) complexes with the morph-C_6H_4-terpy ligand (**1A** and **2A**) exhibited significantly reduced HOMO–LUMO gaps relative to their reference complexes (**1B** and **2B**). The HOMO–LUMO energy gap decreased in the order of **2B** (4.20 eV) > **1B** (3.74 eV) > **1A** (3.23 eV) > **2A** (2.87 eV).

Notably, the replacement of three electron-donating halide ions in [$IrCl_3$(R-C_6H_4-terpy-κ^3N)] by the π-accepting R-C_6H_4-terpyκ^3N ligand in [Ir(R-C_6H_4-terpy-κ^3N)$_2$]$^{3+}$resulted in the stabilization of the HOMO and LUMO levels of the bis-terpyridyl systems. In the pairs **1A**–**2A** and **1B**–**2B**, the HOMO energy decreased by ~0.22 eV and ~1.1 eV, respectively. In turn, the LUMO energy of **1A** and **1B** dropped by ~0.58 eV and ~0.64 eV compared to **2A** and **2B**, respectively.

As expected, the morpholine substituent also altered the nature of the HOMO orbital. Unlike the HOMO of **1B**, which predominantly comprised the orbitals of the Ir(III) center (61.8 %) and chloride ions (27.4 %), the HOMO of **1A** was a combination of morpholine (32.1%), phenylene (48.1%), and terpy (9.5%) orbitals. Compared to **1B**, the metal character of the HOMO of **1A** decreased from 61.8 % to 8.5 %. The highest occupied molecular orbitals of **2A** and **2B** resided almost exclusively on the R-C_6H_4-terpy ligand. For morpholinyl-substituted complex (**2A**), it comprised the morpholine group (35.9 %) and phenylene linker (46.5%). The metal contributions in the HOMO of **2A** and **2B** were 2.1% and 12.5%, respectively. The lowest unoccupied molecular orbital of all the studied Ir(III) complexes was predominately constituted by π* orbitals of the terpy backbone.

4. Photophysical Properties–Experimental and Theoretical Insights

The electronic absorption properties of [$IrCl_3$(R-C_6H_4-terpy-κ^3N)] and [Ir(R-C_6H_4-terpy-κ^3N)$_2$](PF_6)$_3$ were studied in MeCN and DMSO (Figures 5 and S8). The complexes **1** and **2** showed insufficient solubility in less polar solvents. The absorption band maxima and molar extinction coefficients of **1**–**2** are summarized in Table S8.

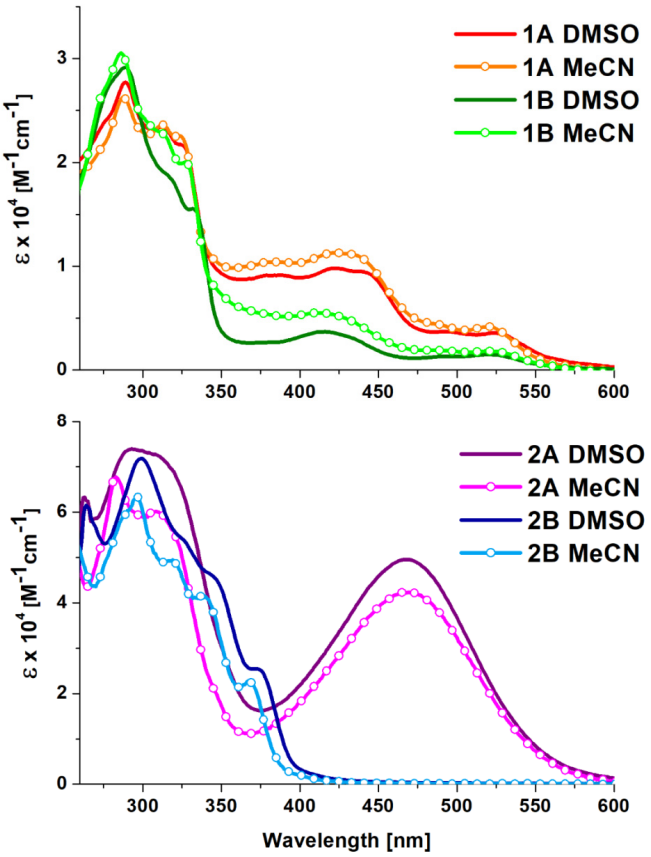
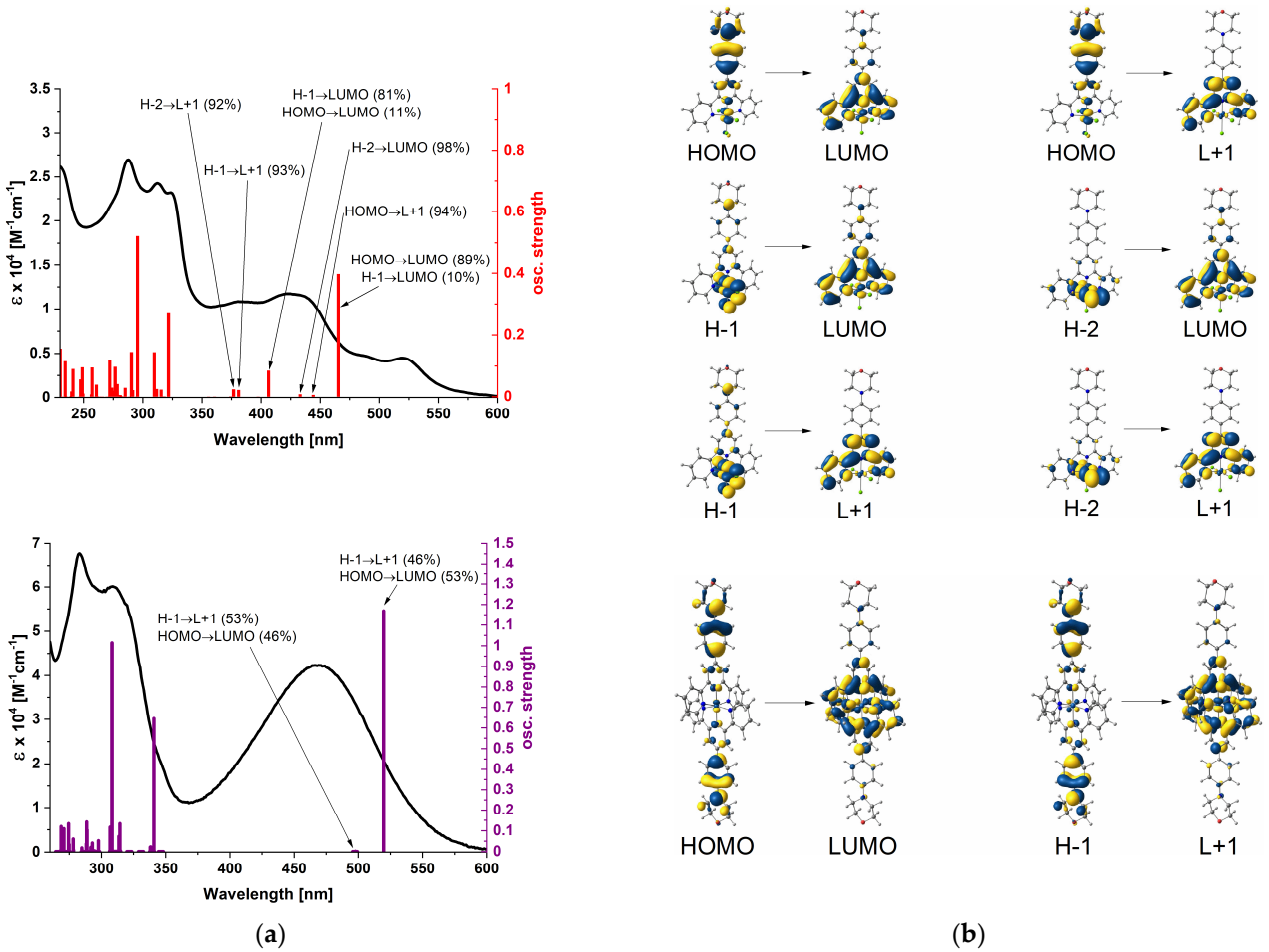


Figure 5. UV–Vis spectra of Ir(III) complexes recorded in MeCN and DMSO solutions.

As demonstrated in Figure 5, the model complex **1B** exhibited intense high-energy absorption bands in the range of 225–350 nm, which were attributed to π–π* transitions of the Ph-terpy ligand, and noticeably weaker absorptions with maxima above 350 nm, which were tentatively assigned to charge-transfer transitions ^{1}MLLCT with a possible admixture of spin-forbidden singlet-triplet ^{3}MLLCT due to the high spin-orbit coupling constant of iridium [46–48]. In contrast, the complex **2B** principally absorbed wavelengths below 400 nm. As previously established for related systems [37,41,49–52], these UV bands of **2B** were predominantly attributed to ^{1}IL transitions within the coordinated Ph-terpy ligands. The very low magnitudes of molar extinction coefficients for the absorptions of **2B** in the visible region (Table S8 and Figure S8) are consistent with spin-forbidden singlet-triplet ^{3}MLCT transitions [49,53].

Within the series [$IrCl_3$(R-C_6H_4-terpy-κ^3N)], the attachment of the electron-donating morpholinyl group to the phenyl ring of 2,2′:6′,2″-terpyridine evoked a minor effect on the absorption energies but led to a significant enhancement of the molar extinction coefficients of absorptions bands in the range of 350–550 nm (Table S8 and Figure 5). In contrast, dramatic changes in the absorption characteristics were observed for **2A** in relation to **2B**. The morpholinyl-substituted complex (**2A**) was deeply red and displayed a very strong absorption tailing up to 600 nm, which was absent in the UV–Vis spectrum of its parent chromophore **2B**, which was pale yellow in solution. The molar extinction coefficient of this band exceeded 4 × 10^4 M^{-1}·cm^{-1} in solution.

The character of electronic transitions underlying the absorption features of [$IrCl_3$(R-C_6H_4-terpy-κ^3N)] and [Ir(R-C_6H_4-terpy-κ^3N)$_2$]$(PF_6)_3$ was also investigated theoretically at the DFT/PCM/PBE0/SDD/def2-TZVP level (Figure 6). The calculations confirmed that the changes in the absorption characteristics of the morpholinyl-substituted Ir(III) complexes (**1A** and **2A**) relative to the parent chromophores (**1B** and **2B**) were due to the involvement of ^{1}ILCT transitions, occurring from the electron-donating morpholinyl group to the π-acceptor terpy unit. The low-energy absorptions (above 350 nm) of **1A** mainly originated from the excitations HOMO→LUMO, HOMO→L + 1, H–1→LUMO, H–1→L + 1, H-2→LUMO, and H–2→L + 1. Based on the percentage composition of the molecular orbitals, the transitions HOMO→LUMO and HOMO→L + 1 can be designated as ^{1}ILCT/^{1}IL, while the other ones correspond to the ^{1}MLLCT excitations. The low-energy absorptions of **1B** only comprised ^{1}MLLCT transitions (Table S6). Some discrepancies between the experimental and theoretical electronic spectra of **1A** and **1B** in the low energy part may be rationalized by the possible involvement of spin-forbidden singlet-triplet transitions, which are evidenced by the TD-DFT calculations [46]. The strong visible absorption of **2A** was dominated by the transitions HOMO→LUMO and HOMO–1→LUMO + 1 of prevailing ILCT nature. Both HOMO and HOMO-1 comprised the morpholine group and phenylene linker, while LUMO and LUMO + 1 resided predominately on the terpy backbone.



(**a**) (**b**)

Figure 6. Experimental absorption spectra (black line) of **1A** and **2A** alongside vertical lines presenting singlet–singlet transitions with corresponding oscillator strengths, computed at the TD-DFT/PCM/PBE0/SDD/def2-TZVP level with the use of the PCM model at polarities corresponding to MeCN (**a**); electron density distributions plots of frontier low energy transitions (**b**). The data for parent compounds **1B** and **2B** are provided in Table S6 in the Supplementary Materials.

Prior to the investigations of the excited-state properties of **1**–**2**, their stability and photostability in solution were confirmed by UV–Vis spectroscopy, as demonstrated in Figures S9 and S10. The photoluminescence properties of the Ir(III) complexes were explored in MeCN and DMSO solutions at room temperature (RT), in a solid state, and in a frozen matrix of EtOH/MeOH (4:1 *v*/*v*) at 77 K, as presented in Figure 7 and Table 2. Some additional photophysical data of **1**–**2** are provided in the Supplementary Materials (Figures S11–S18).

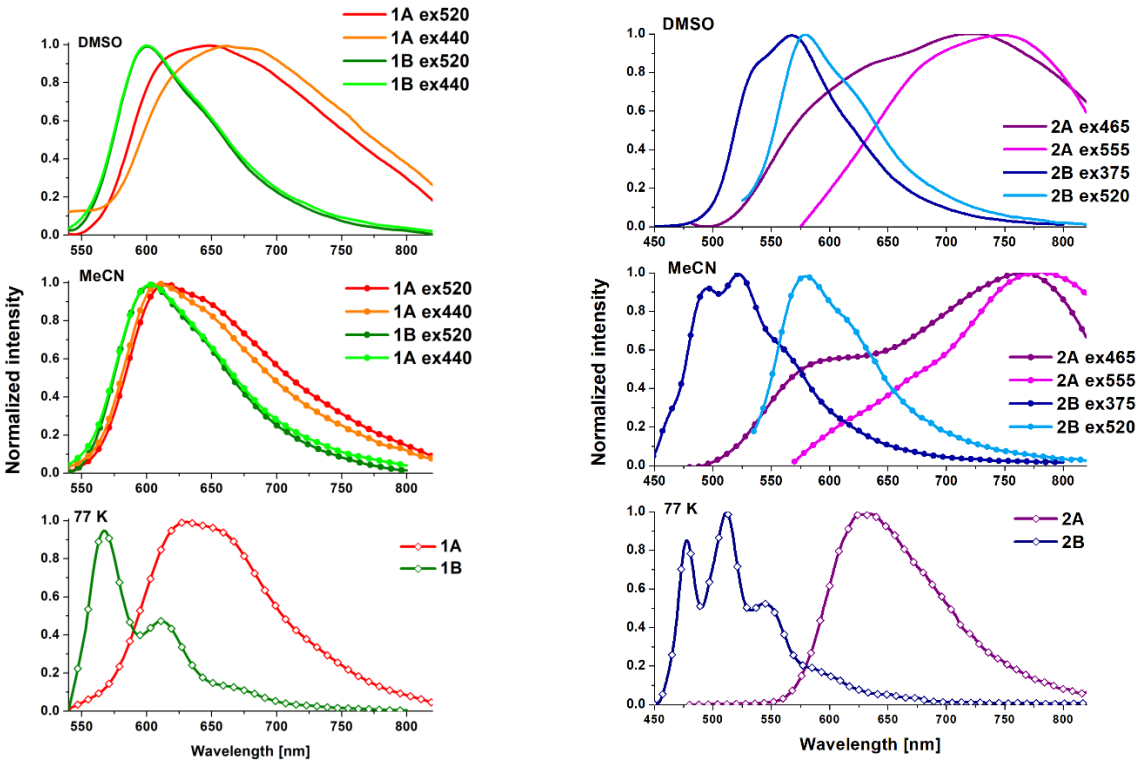


Figure 7. Normalized emission spectra of pairs **1A**–**1B** and **2A**–**2B** in DMSO and MeCN solutions at RT, and MeOH/EtOH (1:4 *v*:*v*) rigid matrix at 77 K.

Table 2. Summary of luminescence properties of **1A**–**1B** and **2A**–**2B**.

Medium	Compound	λ_{ex} [a] [nm]	λ_{em} [b] [nm]	τ_{av} [c] [μs]	Φ [d] [%]	Compound	λ_{ex} [nm]	λ_{em} [nm]	τ_{av} [μs]	Φ [%]
77 K	**1A**	520	639	10.90	–	**1B**	520	565	12.43	–
DMSO		440/520	670/650	1.22	3.74		440/520	600	1.75	37.80
MeCN		440/520	611/614	1.45	1.63		440/520	604	1.96	5.86
solid		530	710	0.21	4.38		525	745	0.21	2.48
77 K	**2A**	465	632	90.45	–	**2B**	370	512	40.08	–
DMSO		465/555	720/750	0.10	7.40		375/520	567/578	4.46	4.22
MeCN		465/555	765/780	0.07	0.16		375/520	522/580	6.50	10.18
solid		500	735	0.58	<0.05		500	600	10.30	4.99

[a] λ_{ex}—excitation wavelength; [b] λ_{em}—emission wavelength; [c] τ_{av}—average lifetime of luminescence; [d] Φ–quantum yield.

For all the studied complexes, their lifetimes were in the microsecond or sub-microsecond domain (Table 2), and the photoluminescence intensities and lifetimes were sensitive to oxygen quenching, supporting the idea that the observed emission originates from a triplet excited state (Figures S11 and S12).

The complexes **1A** and **1B** in deaerated MeCN and DMSO solutions showed unstructured emission bands. Compared to the model chromophore **1B**, the phosphorescence band of **1A** was noticeably broader and appeared at a lower energy, with the emission maximum red-shifted by 50 nm for the DMSO solution and 10 nm for MeCN upon excitation at 520 nm. A bathochromic shift in the emission maximum of **1A** was accompanied by a slight decrease in the excited-state lifetime relative to **1B** (Table 2).

In contrast to **1B**, which showed excitation-independent emission, the energy of the emission of **1A** was affected by excitation wavelengths, becoming noticeably red-shifted upon wavelength excitations in the range of 400–525 (Figure S13). A difference between **1A** and **1B** was also noticed when the frozen-state emissions were considered. Upon cooling to 77 K, the emission band of **1A** remained structureless and appeared almost in the same range as the RT emission band, while the frozen-state emission band of **1B** exhibited well-resolved vibronic progressions and appeared at a higher energy in relation to that in solution, as shown in Figure 7. All these findings indicate that the complex **1B** emits from a triplet excited state of ^{3}MLLCT character with a minor contribution of $^3\pi\rightarrow\pi^*_{terpy}$ transitions (^{3}IL), while the emissive triplet excited state of the morpholinyl-substituted Ir(III) analog (**1A**) has a mixed nature ^{3}MLLCT–^{3}ILCT. By analogy to previous findings [14,29–36], the contribution of ^{3}ILCT in the triplet excited state of **1A** manifested in a bathochromic shift of the emission in solution at RT and frozen matrix EtOH/MeOH relative to the parent chromophore. Transition metal complexes functionalized with electron-rich groups, which emit from the ^{3}MLLCT excited state, are expected to show a hypsochromic shift compared to the unsubstituted model compounds [14,29].

For the bis-terpyridyl iridium(III) complexes, the morpholinyl group induced dramatic changes in the emission characteristics (Figures 7 and S14–S17). In solution at RT, the model chromophore **2B** displayed a green emission. Its emission band exhibited a weak vibronic structure, which became well resolved upon cooling to 77 K. The frozen-state emission band of **2B** appeared almost in the same range as that in MeCN at RT upon excitations of $\leq$375 nm, but it was slightly blue-shifted in relation to its emission in DMSO (Figures 7 and S14). The differences in the emission energies and spectral profiles of **2B** in MeCN and DMSO can be rationalized by the fact that the emission of [Ir(R-terpy-κ^3N)$_2$](PF$_6$)$_3$ systems in solution may occur from the triplet excited state of the cation [Ir(R-terpy-κ^3N)$_2$]$^{3+}$ and ion-pair adduct [Ir(R-terpy-κ^3N)$_2$]$^{3+}\cdot$PF$_6^-$ [41,50,54–57]. While the emission of **2B** in MeCN upon excitations of $\leq$375 nm can be attributed to the phosphorescence of [Ir(R-terpy-κ^3N)$_2$]$^{3+}$, the ion-pair formation quenches the phosphorescence of [Ir(R-terpy-κ^3N)$_2$]$^{3+}$ in DMSO. The observed emission of **2B** in DMSO originated mainly from the ion-pair adduct [Ir(R-terpy-κ^3N)$_2$]$^{3+}\cdot$PF$_6^-$. In acetonitrile solution, the emission from the ion-pair adduct occurred using longer excitation wavelengths (Figure S14), as previously reported for the related complex [Ir(terpy-κ^3N)$_2$](PF$_6$)$_3$ [57]. It is worth noting that there were also two alternative explanations of the photoluminescence behavior of [Ir(R-terpy-κ^3N)$_2$]$^{3+}$ cations in previous reports. The emission properties of such systems are attributed to the triplet ligand-centered (^{3}IL) or mixed ^{3}IL–^{3}MLCT excited states [39]. Regarding the first assignment, the lack of the strong vibronic progression of the emission band at RT, typical of ^{3}IL emission, is rationalized by the thermal distribution of conformers with different torsion angles between the terpy core and aryl pendant group, leading to a less well-resolved emission band [39]. The transient absorption findings, discussed in the next section, indicate that the emission of **2B** is not of pure of ^{3}IL phosphorescence, but rather occurs from the triplet excited state of the mixed ^{3}IL–^{3}MLCT character.

The emission spectrum of the morpholinyl-substituted complex (**2A**) was dominated by the structureless band in the NIR region, with the maximum at 760 nm in MeCN and 750 nm in DMSO, red-shifted by ~240 and 180 nm relative to the model complex **2B**,

respectively. A bathochromic shift in the emission of **2A** was accompanied by a noticeable decrease in the excited-state lifetime relative to **2B** (Table 2). The shoulder/band at higher energies of **2A** can be assigned the reabsorption or emission from the ^{3}MLLCT excited state (Figure S14). The frozen-state emission of **2A** remained non-structured and occurred in a higher energy region (630 nm) compared to its room-temperature emission. The photoluminescence characteristics of **2A** are typical of the emission occurring from ^{3}ILCT excited state [58–61]. It is worth noting that NIR emitters are of high significance due to their potential applications in biomedical imaging [62–64].

The photoluminescence properties of **1**–**2** were also investigated in the solid state. As demonstrated in Figure 8, the solid-state triplet emission band of **2B** occurred in a higher energy region (orange-yellow) and was characterized by a noticeably prolonged lifetime (~10 μs) compared to other studied complexes, showing emission in the red wavelength range, with lifetimes in the sub-microsecond domain (Table 2).

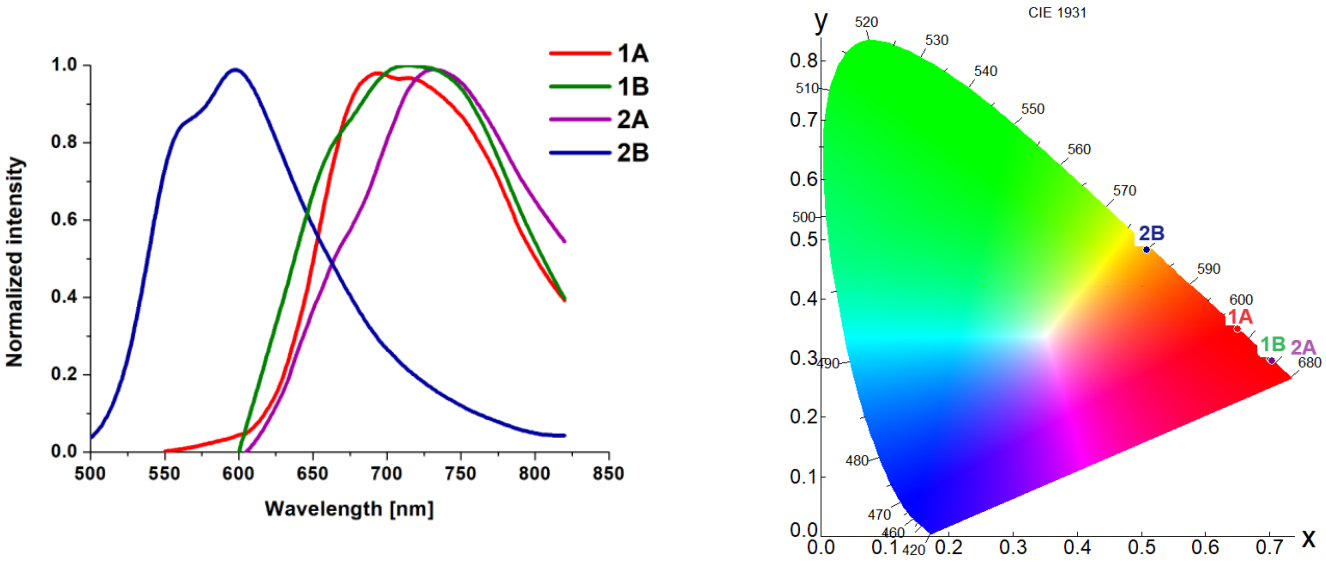


Figure 8. Normalized emission spectra of pairs **1A**–**1B** and **2A**–**2B** in the solid state alongside the CIE chromaticity diagram.

To theoretically investigate the excited-state properties of complexes **1**–**2**, their geometries were optimized in triplet states (T_1) and triplet energies were calculated from the energy difference between the ground singlet and triplet excited states $\Delta E_{T_1-S_0}$. The theoretically determined triplet emissions, 694 nm for **1A**, 590 nm for **1B**, 832 nm for **2A**, and 540 nm for **2B**, are in satisfactory agreement with the experimental values (Tables 2 and S7). Regarding the spin density surface plots (Figures 9 and S7), the emission in the complexes **1A**, **1B**, **2A**, and **2B** occurred due to the triplet excited state of an MLCT-ILCT, MLLCT, ILCT, and IL-MLCT nature, respectively.

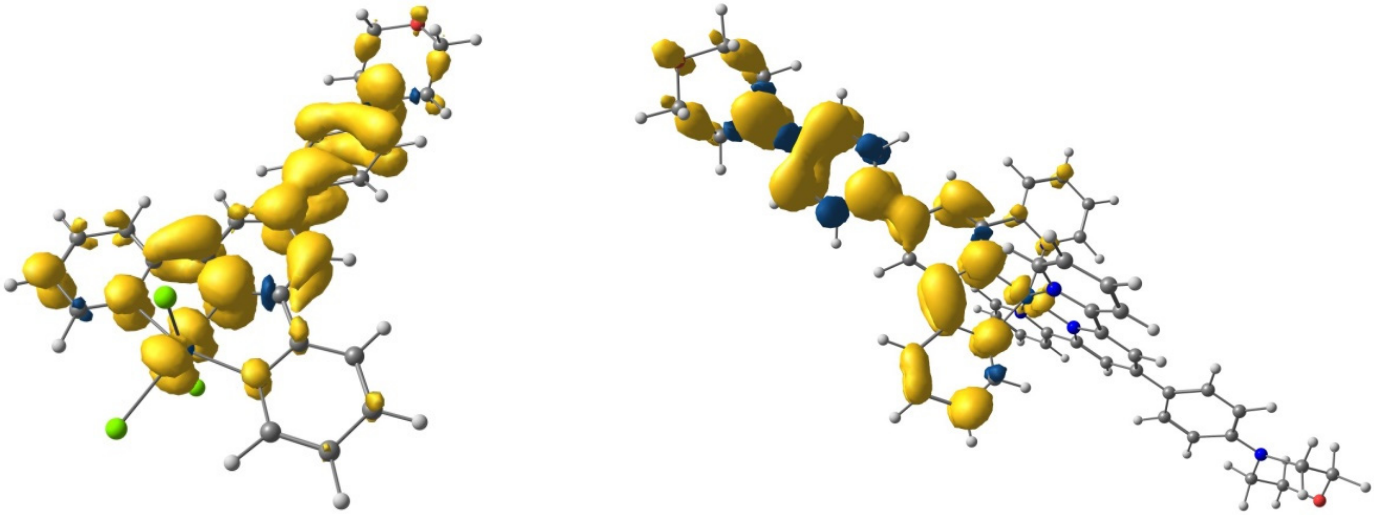


Figure 9. Spin density surface plots for **1A** and **2A**. For parent chromophores, spin density surface plots are provided in the Supplementary Materials.

5. Femtosecond Transient Absorption Spectra

To further understand the triplet excited state characteristics of the studied complexes, femtosecond transient absorption (fs-TA) measurements were recorded in deaerated DMSO (**1A** and **1B**) and MeCN (**2A** and **2B**) solutions upon excitation at 355 nm. TA solutions were prepared at concentrations of 50–250 μM to provide an absorbance of ~0.5 in 2 mm path length quartz cells at the excitation wavelength. The results of the fs-TA measurements and global fitting analyses are summarized in Figure 10 and Figures S19–S23. The photostability of the Ir(III) complexes during the TA experiments was verified by comparing their UV–Vis spectra recorded before and after irradiation (Figure S24).

The complexes **1A** and **2A** exhibited distinct transient absorption (TA) features compared to their parent chromophores (**1B** and **2B**), indicating that the introduction of the electron-donating morpholinyl group significantly affected the nature of the lowest triplet excited state of [$IrCl_3$(R-C_6H_4-terpy-κ^3N)] and [Ir(R-C_6H_4-terpy-κ^3N)$_2$](PF_6)$_3$. Specifically, **1A** and **2A** displayed ground-state bleaching (GSB) in wavelength regions corresponding to their visible charge-transfer absorptions, along with excited-state absorption bands (ESA) in the ranges of 375–415 nm and 522–670 nm for **1A**, and 375–425 nm and 540–670 nm for **2A**. In contrast, the TA spectra of the parent chromophores displayed only positive bands across the UV and visible regions, indicating that **1B** and **2B** have a stronger triplet excited-state absorption than the ground-state absorption [65–68]. For all the studied Ir(III) complexes, the TA signals appeared promptly after photoexcitation at 355 nm. After vibrational cooling, solvation, and geometrical relaxation within the triplet manifold, these signals persisted up to the end of the delay stage (7 ns). Ultrafast intersystem crossing occurs on a time scale shorter than the instrument response and is not detected with our experimental setup [48].

The comparison of the TA spectral profiles of **2A** and **2B** (Figure S23) indicated the involvement of different triplet excited states in their transient absorptions. For complex **2A**, the TA spectra comprised two ESA bands separated by a strong GSB signal, with two well-defined isosbestic points at 425 and 540 nm. The decay of both ESA bands and the recovery of the GSB occurred on the same time scale. The ESA band in the UV range was attributed to the terpyridyl anion radical [69,70], associated with the ^{3}ILCT excited state, represented by the ESA with a maximum at 645 nm. The triplet excited state was of a predominantly ^{3}ILCT nature.

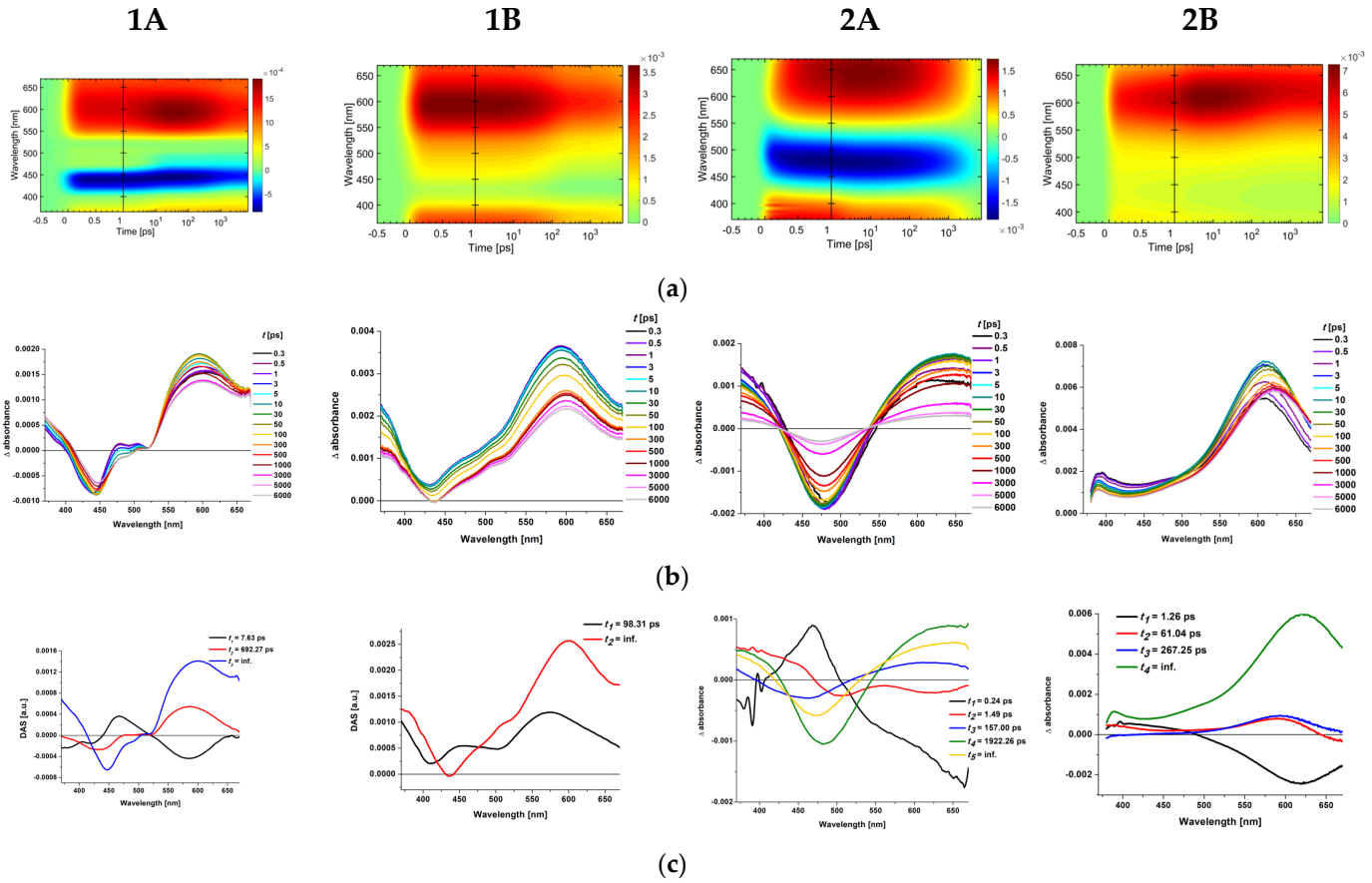


Figure 10. The results of fs-TA measurements and global fitting analyses: (**a**) 2D time–wavelength plots; (**b**) fs-TA spectra at selected time delays (ps); (**c**) decay-associated spectra DAS_i with appropriate time constant t_i (see also Figures S19–S22).

The fs-TA data of **2B** indicated a mixed ^{3}IL-^{3}MLCT nature. With reference to the TA findings for [Ir(terpy-κ^{3}N)$_2$](PF$_6$)$_3$ [51], the higher energy TA signal suggests a $^3IL_{terpy}$ triplet excited state, while the lower energy one can be assigned to the ^{3}MLCT transient absorption. The presence of two different transient species undergoing interconversion was supported by the isosbestic point at 515 nm in the TA spectrum of **2B**. Additionally, the lower energy ESA band of **2A** was similar to the low energy ESA band of the model chromophore **1B**, characterized by the lowest triplet excited state of a ^{3}MLLCT nature (Figure S23).

The comparison of the TA spectral profiles of **1A** and **1B** (Figure S23) demonstrated that the morpholinyl group induces smaller variations in the TA spectral features of [IrCl$_3$(R-C$_6$H$_4$-terpy-κ^{3}N)]. The presence of a GSB band, the broadening of the visible ESA band, and different decay kinetics relative to **1B** suggest that the TA spectral features of **1A** correspond to a triplet excited state of a mixed ^{3}MLLCT-^{3}ILCT nature, with a dominant contribution of the first component.

6. Conclusions

The work presents comprehensive studies of [IrCl$_3$(morph-C$_6$H$_4$-terpy-κ^{3}N)] (**1A**), [Ir(morph-C$_6$H$_4$-terpy-κ^{3}N)$_2$](PF$_6$)$_3$ (**2A**), [IrCl$_3$(Ph-terpy-κ^{3}N)] (**1B**), and [Ir(Ph-terpy-κ^{3}N)$_2$](PF$_6$)$_3$ (**2B**), which were designed to explore the impact of the electron-donating morpholinyl (morph) group on the ground- and excited-state properties of two different types of Ir(III) complexes: [IrCl$_3$(R-C$_6$H$_4$-terpy-κ^{3}N)] and [Ir(R-C$_6$H$_4$-terpy-κ^{3}N)$_2$](PF$_6$)$_3$. We demonstrated that the attachment of morpholine leads to a change in the nature of the singlet and triplet excited states of bis-terpyridyl iridium(III) complexes, switching

from intraligand with a small admixture of metal-to-ligand charge transfer (IL–MLCT) for **2B** to intraligand charge transfer (ILCT) in **2A**. Consequently, the compounds **2A** and **2B** exhibited completely different absorption and emission features. The deeply red complex **2A** displayed very strong absorption tailing up to 600 nm, which was absent in the UV–Vis spectrum of its parent chromophore **2B**, which was pale yellow in solution and predominately absorbed wavelengths below 400 nm. The room-temperature emission of **2A** was red-shifted by ~200 nm and showed a decreased lifetime relative to the model complex **2B**. The optical properties of the mono-terpyridyl iridium(III) complexes were less impacted by the morpholinyl substituent. Only an absorption enhancement in the range of 350–550 nm and a small red shift in the emission were observed for **1A** compared to the model chromophore **1B**. Bases on the static and time-resolved spectroscopic findings, accompanied with theoretical DFT/TD-DFT calculations, the character of the singlet and triplet excited states of **1A** was assigned as a mixed MLLCT-ILCT. The structure–property relationships discussed herein are of high importance for controlling the photophysical characteristics of [$IrCl_3$(R-C_6H_4-terpy-κ^3N)] and [Ir(R-C_6H_4-terpy-κ^3N)$_2$]$(PF_6)_3$, and making further progress in the development of Ir-based luminophores.

7. Experimental

7.1. Materials and Methods

Commercially available iridium(III) chloride salt hydrate, ammonium hexafluorophosphate, 2-acetylpyridine, 4-(4-morpholinyl)benzaldehyde and benzaldehyde were used without further purification. The solvents for the syntheses and spectroscopic measurements were reagent and HPLC grade, respectively. Ligands morph-C_6H_4-terpy and Ph-terpy were prepared through base-mediated Kröhnke condensation from 2-acetylpyridine and two equivalents of the appropriate aldehyde (4-(4-morpholinyl)benzaldehyde for morph-C_6H_4-terpy and benzaldehyde for Ph-terpy, as described previously [31,71]. Elemental analyses were performed using a Vario EL Cube (Elementar) for the C, H, and N content. NMR spectra were recorded on a Bruker Avance 500 NMR spectrometer in DMSO-d_6. IR spectra were acquired using a Nicolet iS5 FTIR spectrophotometer (4000–400 cm^{-1}) using the KBr pellet method. X-ray diffraction data were collected at room temperature using a Gemini A Ultra diffractometer (Oxford Diffraction) with MoKα radiation (λ = 0.71073 Å), and crystallographic data for **1A**, **1B**, and **2B** were deposited with the Cambridge Crystallographic Data Center (CCDC 2359006-2359008). The UV–Vis absorption spectra were recorded on an Evolution 220 (ThermoScientific) UV–Vis spectrometer. The emission and excitation spectra along with the time-resolved TCSPC measurements at room temperature and in 77 K frozen matrix (4:1 *v*/*v*) were measured on an FLS-980 fluorescence spectrophotometer (Edinburgh Instruments). The fs TA spectra were acquired using a pump-probe transient absorption spectroscopy system (Ultrafast Systems, Helios). Theoretical calculations were performed using the GAUSSIAN-16 (Rev. C.01) program package [44] at the DFT or TD-DFT level with the PBE0 [72–74] functional. The basis sets used were Stuttgart Relativistic Small Core ECP with the corresponding pseudopotentials [45,75] for iridium (obtained from Basis Set Exchange Database [76]) and def2-TZVP for other elements [45,77]. A more extended experimental description is provided in the Supplementary Materials.

7.2. Preparation of Ir(III) Complexes

[$IrCl_3$(R-C_6H_4-terpy-κ^3N)]: A mixture of $IrCl_3 \cdot xH_2O$ (0.30 g; 1 mmol) and the appropriate R-terpy ligand (1 mmol) in degassed methoxyethanol was placed in a 25 mL Teflon-lined hydrothermal synthesis autoclave reactor and heated at 120 °C for 24 h. After that, the autoclave was gradually cooled to room temperature (24 h). The resulting reddish-brown crystalline precipitate was collected by filtration; washed with acetonitrile, chloroform, and diethyl ether; and dried in air.

[$IrCl_3$(morph-C_6H_4-terpy-κ^3N)] (1A): Yield: 0.48 g, 70%. **Anal. calc**. for $C_{25}H_{22}Cl_3IrN_4O$ (693.04 g/mol): C 43.33 H 3.20, N 8.08% found: C 43.50; H 3.03; N 8.43%. **^{1}H NMR** (500 MHz, DMSO-d_6) ^{1}H NMR (500 MHz, DMSO-d_6) δ = 9.22 (dd, *J* = 5.8, 1.6 Hz, 1H), 9.04

(s, 1H), 8.92 (d, *J* = 8.1 Hz, 1H), 8.29 (td, *J* = 7.8, 1.6 Hz, 1H), 8.17 (d, *J* = 9.0 Hz, 1H), 7.96 (ddd, *J* = 7.6, 5.5, 1.4 Hz, 1H), 7.20 (d, *J* = 9.1 Hz, 1H), 3.81–3.79 (m, 2H), 3.38–3.36 (m, 2H) ppm. **^{13}C NMR** (126 MHz, DMSO-d_6) δ = 159.93, 157.44, 153.45, 151.20, 140.56, 129.62, 128.63, 125.62, 124.64, 119.59, 114.87 ppm. ^{31}P NMR (202 MHz, DMSO-d_6) δ = −133.56–(−154.64) (m, $\underline{P}F_6^-$) ppm. **IR (KBr, cm^{-1})** intensity: s—strong, m—medium, w—weak: 3449 (w), 3060 (w), 2952 (w), 2844 (w), 1596 (s), 1529 (m), 1474 (w), 1446 (w), 1414 (m), 1385 (w), 1305 (w), 1265 (w), 1230 (s), 1220 (s), 1119 (m), 1051 (w), 930 (m), 883(w), 814 (w), 791 (m), 762 (w), 725 (w), 568 (w), 523 (w), 454 (w).

[IrCl$_3$(Ph-terpy-κ^{3}N)] (**1B**): Yield: 0.110 g, 55%. **Anal. calc**. for $C_{21}H_{15}Cl_3IrN_3$ (607.94 g/mol): C 41.49, H 2.49, N 6.91% found: C 40.27; H 2.78; N 6.70%. **^{1}H NMR** (500 MHz, DMSO-d_6) δ = 9.22 (dd, *J* = 5.6, 1.6 Hz, 1H), 9.11 (s, 1H), 8.92 (d, *J* = 8.1 Hz, 1H), 8.31 (td, *J* = 7.8, 1.6 Hz, 1H), 8.21 (dd, *J* = 7.2, 1.4 Hz, 1H), 7.98 (ddd, *J* = 7.2, 5.6, 1.4 Hz, 1H), 7.71 (t, *J* = 7.7 Hz, 1H), 7.61 (t, *J* = 7.4 Hz, 1H) ppm. **^{13}C NMR** (126 MHz, DMSO-d_6) δ = 159.68, 159.07, 157.84, 155.95, 153.49, 153.38, 142.67, 140.73, 135.16, 130.32, 129.91, 129.72, 128.84, 128.81, 128.76, 127.46, 125.85, 123.03, 122,11, 121.56 ppm. ^{31}P NMR (202 MHz, DMSO-d_6) δ = −133.55–(−154.63) (m, $\underline{P}F_6^-$) ppm. **IR (KBr, cm^{-1})** intensity: vs—very strong; s—strong, m—medium, w—weak: 3441 (m), 3047 (m), 1605 (s), 1547 (w), 1475 (m), 1451 (w), 1413 (s), 1304 (w), 1246(w), 1233 (m), 1161 (m), 1103 (w), 1051 (w), 1030 (w), 890 (m), 790 (s), 768 (s), 729 (w), 691 (m), 655 (w), 646 (w), 626 (w), 505 (w), 479 (m), 455 (w).

[Ir(R-C$_6$H$_4$-terpy-κ^{3}N)$_2$](PF$_6$)$_3$: A mixture of [IrCl$_3$(R-C$_6$H$_4$-terpy-κ^{3}N)] (0.1 mmol) and the appropriate R-C$_6$H$_4$-terpy ligand (0.125 mmol) in ethylene glycol (8 mL) was heated at 180 °C (oil bath) in an argon atmosphere overnight. Subsequently, a clear solution was cooled to room temperature, and a saturated aqueous solution of $(NH_4)_2PF_6$ was added dropwise, leading to a reddish-brown (**2A**) and yellow-orange (**2B**) precipitate. After stirring for 8 h, the obtained precipitate was filtered, washed with water and diethyl ether, and dried in air. The crude products of **2A** and **2B** were purified by crystallization from the dichloromethane–methanol mixture.

[Ir(morph-C$_6$H$_4$-terpy-κ^{3}N)$_2$](PF$_6$)$_3$ (**2A**): Yield: 0.064 g, 45%. **Anal. calc**. for $C_{50}H_{44}F_{18}IrN_8O_2P_3 \cdot CH_2Cl_2$ (1500.98 g/mol): C 40.81, H 3.09, N 7.47% found: C 41.14; H 2.69; N 7.41%. **^{1}H NMR** (500 MHz, DMSO-d_6) δ = 9.49 (s, 1H), 9.21 (d, *J* = 8.4 Hz, 1H), 8.45 (d, *J* = 9.0 Hz, 1H), 8.35 (td, *J* = 7.9, 1.5 Hz, 1H), 7.95 (dd, *J* = 5.7, 1.5 Hz, 1H), 7.55 (ddd, *J* = 7.5, 5.7, 1.4 Hz, 1H), 7.31 (d, *J* = 9.1 Hz, 1H), 3.84 (t, *J* = 4.9 Hz, 2H), 3.47 (t, *J* = 4.9 Hz, 2H) ppm. **^{13}C NMR** (126 MHz, DMSO-d_6) δ = 159.04, 154.45, 153.93, 153.86, 153.61, 142.77, 129.98, 129.77, 127.41, 123.70, 121.61, 118.55, 114.61, 66.41, 47.27 ppm. **IR (KBr, cm^{-1})** intensity: vs—very strong; s—strong, m—medium, w—weak: 3422 (m), 3086 (w), 2853 (w), 1592 (s), 1527 (w), 1478 (m), 1465 (m), 1449 (m), 1419 (m), 1361 (s), 1298 (w), 1232 (s), 1213 (s), 1114 (m), 1048 (m), 1032 (m), 928 (m), 839 (vs), 785 (m), 755 (w), 645 (w), 558 (s).

[Ir(Ph-terpy-κ^{3}N)$_2$](PF$_6$)$_3$ (**2B**): Yield: 0.081 g, 65%. **Anal. calc**. for $C_{42}H_{30}F_{18}IrN_6P_3 \cdot CH_2Cl_2$ (1330.77 g/mol): C 38.81, H 2.42, N 6.32% found: C 39.19; H 2.13; N 6.35%. **^{1}H NMR** (500 MHz, DMSO-d_6 δ = 9.62 (s, 2H), 9.23 (dd, *J* = 8.2, 0.7 Hz, 2H), 8.46 (d, *J* = 7.2 Hz, 2H), 8.38 (td, *J* = 7.9, 1.4 Hz, 2H), 7.96 (dd, *J* = 5.7, 0.8 Hz, 2H), 7.85 (t, *J* = 7.6 Hz, 2H), 7.77 (t, *J* = 7.4 Hz, 1H), 7.58 (ddd, *J* = 7.5, 5.7, 1.4 Hz, 2H) ppm. **^{13}C NMR** (126 MHz, DMSO-d_6) δ = 158.69, 154.96, 154.46, 153.79, 142.97, 135.20, 132.40, 130.08, 129.96, 128.80, 127.69, 123.99, 118.55 ppm. **IR (KBr, cm^{-1})** intensity: vs—very strong; s—strong, m—medium, w—weak: 3789 (w), 3661 (w), 3432 (m), 3126 (m), 2250 (w), 1610 (s), 1556 (m), 1479 (s), 1454 (w), 1421 (s), 1244 (m), 1170 (m), 1103 (w), 1061 (w), 1034 (w), 1018(w), 977 (w), 896 (w), 838 (vs), 789 (w), 768 (s), 728 (w), 692 (m), 644(w), 558 (s), 498 (w).

Supplementary Materials: Crystallographic data for **1A**, **1B** and **2B** were deposited with the Cambridge Crystallographic Data Center, CCDC 2359006-2359008. Copies of this information may be obtained free of charge from the Director, CCDC, 12 Union Road, Cambridge CB2 1EZ, UK (Fax: +44 1223 336033; e-mail: deposit@ccdc.cam.ac.uk or www.ccdc.cam.ac.uk). The following supporting information can be downloaded at: https://www.mdpi.com/article/10.3390/molecules29133074/s1, Figures S1–S4: ^{1}H and ^{13}C NMR spectra; Figure S5: IR spectra; Table S1: Crystal data and structure

refinement; Table S2: Short intra- and intermolecular contacts; Table S3: Short π●●●π ring interactions; Table S4: P—F●●● π-ring interactions for **2B**; Figure S6: View of 3D supramolecular structure of **1B** resulting from weak π●●●π interactions; Table S5: Experimental and theoretical bond lengths and angles; Table S6: Assignment of electron excitations computed at TD-DFT/PCM/PBE0/SDD/def2TZVP level to acetonitrile UV–Vis absorptions; Table S7: Triplet energies; Figure S7: Spin density surface plots; Table S8: The absorption maxima and molar extinction coefficient values; Figure S8: The absorption spectra of **2B** recorded at 2.5×10^{-5} and 5×10^{-4} mol/dm^3 concentrations; Figure S9: The photostability in DMSO and MeCN solutions; Figure S10: The kinetic stability; Figures S11 and S12: The emission spectra and decay curves in aerated and deaerated solutions: Figures S13 and S14: Excitation-dependent emission; Figures S15–S17: Absorbance, excitation, and emission steady-state spectra of **1**–**2** with the corresponding decay curves; Figure S18: Decay curves of **1**–**2** in solid state; Figures S19–S23: Summary of the TA analysis; Figure S24: The photodamage tests. References [31,44,45,75–82] has been cited the in the Supplementary Materials.

Author Contributions: The manuscript was prepared through the contributions of all authors. B.M. and J.P.-G. conceptualized, designed, and supervised the research. M.P. carried out the synthesis of the organic ligands and NMR analysis. B.M. and J.P.-G. performed the synthesis of the Ir(III) complexes and X-ray single crystal analysis. J.P.-G., A.K. (Aleksandra Kwiecień) and A.K. (Anna Kryczka) performed the steady-state spectroscopic measurements, while K.C. computed the theoretical calculations. J.P.-G. performed the time-resolved spectroscopic measurements. J.P.-G., A.K. (Aleksandra Kwiecień) and K.C. prepared the figures in the paper and Supplementary Materials files. B.M. and J.P.-G. wrote the manuscript with contributions from all authors. All authors have read and agreed to the published version of the manuscript.

Funding: This work was financed by the funds granted under the Research Excellence Initiative of the University of Silesia in Katowice.

Institutional Review Board Statement: Not applicable.

Informed Consent Statement: Not applicable.

Data Availability Statement: Data are contained within the article and Supplementary Materials.

Acknowledgments: The calculations were carried out in the Wroclaw Centre for Networking and Supercomputing (http://www.wcss.wroc.pl, accessed on 1 June 2024). The authors would like to thank inż Mariola Siwy for the elemental analysis.

Conflicts of Interest: The authors declare no conflicts of interest.

References

1. Wei, C.; He, Y.; Shi, X.; Song, Z. Terpyridine-Metal Complexes: Applications in Catalysis and Supramolecular Chemistry. *Coord. Chem. Rev.* **2019**, *385*, 1–19. [CrossRef]
2. Rupp, M.T.; Shevchenko, N.; Hanan, G.S.; Kurth, D.G. Enhancing the Photophysical Properties of Ru(II) Complexes by Specific Design of Tridentate Ligands. *Coord. Chem. Rev.* **2021**, *446*, 214127. [CrossRef]
3. Panicker, R.R.; Sivaramakrishna, A. Remarkably Flexible 2,2′:6′,2″-Terpyridines and Their Group 8–10 Transition Metal Complexes—Chemistry and Applications. *Coord. Chem. Rev.* **2022**, *459*, 214426. [CrossRef]
4. Momeni, B.Z.; Abd-El-Aziz, A.S. Recent Advances in the Design and Applications of Platinum-Based Supramolecular Architectures and Macromolecules. *Coord. Chem. Rev.* **2023**, *486*, 215113. [CrossRef]
5. Palion-Gazda, J.; Choroba, K.; Maroń, A.M.; Malicka, E.; Machura, B. Structural and Photophysical Trends in Rhenium(I) Carbonyl Complexes with 2,2′:6′,2″-Terpyridines. *Molecules* **2024**, *29*, 1631. [CrossRef] [PubMed]
6. Momeni, B.Z.; Davarzani, N.; Janczak, J.; Ma, N.; Abd-El-Aziz, A.S. Progress in Design and Applications of Supramolecular Assembly of 2,2′:6′,2″-Terpyridine-Based First Row d-Block Elements. *Coord. Chem. Rev.* **2024**, *506*, 215619. [CrossRef]
7. Breivogel, A.; Kreitner, C.; Heinze, K. Redox and Photochemistry of Bis(Terpyridine)Ruthenium(II) Amino Acids and Their Amide Conjugates—From Understanding to Applications. *Eur. J. Inorg. Chem.* **2014**, *2014*, 5468–5490. [CrossRef]
8. Saccone, D.; Magistris, C.; Barbero, N.; Quagliotto, P.; Barolo, C.; Viscardi, G. Terpyridine and Quaterpyridine Complexes as Sensitizers for Photovoltaic Applications. *Materials* **2016**, *9*, 137. [CrossRef]
9. Kreitner, C.; Mengel, A.K.C.; Lee, T.K.; Cho, W.; Char, K.; Kang, Y.S.; Heinze, K. Strongly Coupled Cyclometalated Ruthenium Triarylamine Chromophores as Sensitizers for DSSCs. *Chem. Eur. J.* **2016**, *22*, 8915–8928. [CrossRef]
10. Mills, I.N.; Porras, J.A.; Bernhard, S. Judicious Design of Cationic, Cyclometalated Ir(III) Complexes for Photochemical Energy Conversion and Optoelectronics. *Acc. Chem. Res.* **2018**, *51*, 352–364. [CrossRef] [PubMed]
11. Liu, P.; Shi, G.; Chen, X. Terpyridine-Containing π-Conjugated Polymers for Light-Emitting and Photovoltaic Materials. *Front. Chem.* **2020**, *8*, 592055. [CrossRef] [PubMed]

12. Laschuk, N.O.; Ebralidze, I.I.; Easton, E.B.; Zenkina, O.V. Osmium- and Cobalt-Terpyridine-Based Electrochromic Devices for "Smart" Signage Application: The Effect of Lighting on Color Perception. *Adv. Electron. Mater.* **2021**, *7*, 2100460. [CrossRef]
13. Genoni, A.; Chirdon, D.N.; Boniolo, M.; Sartorel, A.; Bernhard, S.; Bonchio, M. Tuning Iridium Photocatalysts and Light Irradiation for Enhanced CO_2 Reduction. *ACS Catal.* **2017**, *7*, 154–160. [CrossRef]
14. Fernández-Terán, R.; Sévery, L. Living Long and Prosperous: Productive Intraligand Charge-Transfer States from a Rhenium(I) Terpyridine Photosensitizer with Enhanced Light Absorption. *Inorg. Chem.* **2021**, *60*, 1334–1343. [CrossRef] [PubMed]
15. Wu, A.; Tang, Y.; Li, X.; Zhang, B.; Zhou, A.; Qiao, Z.; Tong, L. A Photofunctional Platform of Bis-Terpyridine Ruthenium Complex-Linked Coordination Polymers with Structural Diversity. *J. Mater. Chem. A* **2022**, *10*, 25063–25069. [CrossRef]
16. Ranjan Jena, S.; Mandal, T.; Choudhury, J. Metal-Terpyridine Assembled Functional Materials for Electrochromic, Catalytic and Environmental Applications. *Chem. Rec.* **2022**, *22*, e202200165. [CrossRef]
17. Saha, S.; Doughty, T.; Banerjee, D.; Patel, S.K.; Mallick, D.; Iyer, E.S.S.; Roy, S.; Mitra, R. Electrocatalytic Reduction of CO_2 to CO by a Series of Organometallic Re(I)-Tpy Complexes. *Dalton Trans.* **2023**, *52*, 15394–15411. [CrossRef]
18. Jacques, A.; Devaux, A.; Rubay, C.; Pennetreau, F.; Desmecht, A.; Robeyns, K.; Hermans, S.; Elias, B. Polypyridine Iridium(III) and Ruthenium(II) Complexes for Homogeneous and Graphene-Supported Photoredox Catalysis. *ChemCatChem* **2023**, *15*, e202201672. [CrossRef]
19. Eryazici, I.; Moorefield, C.N.; Newkome, G.R. Square-Planar Pd(II), Pt(II), and Au(III) Terpyridine Complexes: Their Syntheses, Physical Properties, Supramolecular Constructs, and Biomedical Activities. *Chem. Rev.* **2008**, *108*, 1834–1895. [CrossRef]
20. Grau, J.; Caubet, A.; Roubeau, O.; Montpeyó, D.; Lorenzo, J.; Gamez, P. Time-Dependent Cytotoxic Properties of Terpyridine-Based Copper Complexes. *ChemBioChem* **2020**, *21*, 2348–2355. [CrossRef]
21. Musiol, R.; Malecki, P.; Pacholczyk, M.; Mularski, J. Terpyridines as Promising Antitumor Agents: An Overview of Their Discovery and Development. *Expert Opin. Drug Discov.* **2022**, *17*, 259–271. [CrossRef] [PubMed]
22. Abhijnakrishna, R.; Magesh, K.; Ayushi, A.; Velmathi, S. Advances in the Biological Studies of Metal-Terpyridine Complexes: An Overview from 2012 to 2022. *Coord. Chem. Rev.* **2023**, *496*, 215380. [CrossRef]
23. Li, J.; Wang, Z.; Chen, Z.; Xue, X.; Lin, K.; Chen, H.; Pan, L.; Yuan, Y.; Ma, Z. Silver Complexes with Substituted Terpyridines as Promising Anticancer Metallodrugs and Their Crystal Structure, Photoluminescence, and DNA Interactions. *Dalton Trans.* **2023**, *52*, 9607–9621. [CrossRef] [PubMed]
24. Gil-Moles, M.; Concepción Gimeno, M. The Therapeutic Potential in Cancer of Terpyridine-Based Metal Complexes Featuring Group 11 Elements. *ChemMedChem* **2024**, *19*, e202300645. [CrossRef] [PubMed]
25. Mandal, A.A.; Singh, V.; Saha, S.; Peters, S.; Sadhukhan, T.; Kushwaha, R.; Yadav, A.K.; Mandal, A.; Upadhyay, A.; Bera, A.; et al. Green Light-Triggered Photocatalytic Anticancer Activity of Terpyridine-Based Ru(II) Photocatalysts. *Inorg. Chem.* **2024**, *63*, 7493–7503. [CrossRef] [PubMed]
26. Smoleński, P.; Śliwińska-Hill, U.; Kwiecień, A.; Wolińska, J.; Poradowski, D. Design, Synthesis, and Anti-Cancer Evaluation of Novel Water-Soluble Copper(I) Complexes Bearing Terpyridine and PTA Ligands. *Molecules* **2024**, *29*, 945. [CrossRef] [PubMed]
27. Choroba, K.; Machura, B.; Erfurt, K.; Casimiro, A.R.; Cordeiro, S.; Baptista, P.V.; Fernandes, A.R. Copper(II) Complexes with 2,2′:6′,2″-Terpyridine Derivatives Displaying Dimeric Dichloro−μ–Bridged Crystal Structure: Biological Activities from 2D and 3D Tumor Spheroids to In Vivo Models. *J. Med. Chem.* **2024**, *67*, 5813–5836. [CrossRef] [PubMed]
28. Kröhnke, F. The Specific Synthesis of Pyridines and Oligopyridines. *Synthesis* **1976**, *1976*, 1–24. [CrossRef]
29. Fernández-Terán, R.J.; Sucre-Rosales, E.; Echevarria, L.; Hernández, F.E. Dissecting Conjugation and Electronic Effects on the Linear and Non-Linear Optical Properties of Rhenium(I) Carbonyl Complexes. *Phys. Chem. Chem. Phys.* **2022**, *24*, 28069–28079. [CrossRef]
30. Klemens, T.; Świtlicka-Olszewska, A.; Machura, B.; Grucela, M.; Janeczek, H.; Schab-Balcerzak, E.; Szlapa, A.; Kula, S.; Krompiec, S.; Smolarek, K.; et al. Synthesis, Photophysical Properties and Application in Organic Light Emitting Devices of Rhenium(I) Carbonyls Incorporating Functionalized 2,2′:6′,2″-Terpyridines. *RSC Adv.* **2016**, *6*, 56335–56352. [CrossRef]
31. Klemens, T.; Świtlicka, A.; Szlapa-Kula, A.; Krompiec, S.; Lodowski, P.; Chrobok, A.; Godlewska, M.; Kotowicz, S.; Siwy, M.; Bednarczyk, K.; et al. Experimental and Computational Exploration of Photophysical and Electroluminescent Properties of Modified 2,2′:6′,2″-Terpyridine, 2,6-Di(Thiazol-2-yl)Pyridine and 2,6-Di(Pyrazin-2-yl)Pyridine Ligands and Their Re(I) Complexes. *Appl. Organomet. Chem.* **2018**, *32*, e4611. [CrossRef]
32. Klemens, T.; Świtlicka, A.; Machura, B.; Kula, S.; Krompiec, S.; Łaba, K.; Korzec, M.; Siwy, M.; Janeczek, H.; Schab-Balcerzak, E.; et al. A Family of Solution Processable Ligands and Their Re(I) Complexes towards Light Emitting Applications. *Dyes Pigment.* **2019**, *163*, 86–101. [CrossRef]
33. Klemens, T.; Świtlicka, A.; Szlapa-Kula, A.; Łapok, Ł.; Obłoza, M.; Siwy, M.; Szalkowski, M.; Maćkowski, S.; Libera, M.; Schab-Balcerzak, E.; et al. Tuning Optical Properties of Re(I) Carbonyl Complexes by Modifying Push–Pull Ligands Structure. *Organometallics* **2019**, *38*, 4206–4223. [CrossRef]
34. Maroń, A.M.; Szlapa-Kula, A.; Matussek, M.; Kruszynski, R.; Siwy, M.; Janeczek, H.; Grzelak, J.; Maćkowski, S.; Schab-Balcerzak, E.; Machura, B. Photoluminescence Enhancement of Re(I) Carbonyl Complexes Bearing D–A and D–π–A Ligands. *Dalton Trans.* **2020**, *49*, 4441–4453. [CrossRef] [PubMed]
35. Choroba, K.; Maroń, A.; Świtlicka, A.; Szłapa-Kula, A.; Siwy, M.; Grzelak, J.; Maćkowski, S.; Pedzinski, T.; Schab-Balcerzak, E.; Machura, B. Carbazole Effect on Ground- and Excited-State Properties of Rhenium(I) Carbonyl Complexes with Extended Terpy-like Ligands. *Dalton Trans.* **2021**, *50*, 3943–3958. [CrossRef] [PubMed]

36. Palion-Gazda, J.; Szłapa-Kula, A.; Penkala, M.; Erfurt, K.; Machura, B. Photoinduced Processes in Rhenium(I) Terpyridine Complexes Bearing Remote Amine Groups: New Insights from Transient Absorption Spectroscopy. *Molecules* **2022**, *27*, 7147. [CrossRef] [PubMed]
37. Liu, B.; Monro, S.; Li, Z.; Jabed, M.A.; Ramirez, D.; Cameron, C.G.; Colón, K.; Roque, J.I.; Kilina, S.; Tian, J.; et al. New Class of Homoleptic and Heteroleptic Bis(Terpyridine) Iridium(III) Complexes with Strong Photodynamic Therapy Effects. *ACS Appl. Bio Mater.* **2019**, *2*, 2964–2977. [CrossRef] [PubMed]
38. Moura, N.M.M.; Castro, K.A.D.F.; Biazzotto, J.C.; Prandini, J.A.; Lodeiro, C.; Faustino, M.A.F.; Simões, M.M.Q.; da Silva, R.S.; Neves, M.G.P.M.S. Ruthenium and Iridium Complexes Bearing Porphyrin Moieties: PDT Efficacy against Resistant Melanoma Cells. *Dyes Pigment.* **2022**, *205*, 110501. [CrossRef]
39. Williams, J.A.G.; Wilkinson, A.J.; Whittle, V.L. Light-Emitting Iridium Complexes with Tridentate Ligands. *Dalton Trans.* **2008**, *2008*, 2081–2099. [CrossRef]
40. Qin, Q.-P.; Meng, T.; Tan, M.-X.; Liu, Y.-C.; Luo, X.-J.; Zou, B.-Q.; Liang, H. Synthesis and in Vitro Biological Evaluation of Three 4′-(4-Methoxyphenyl)-2,2′:6′,2″-Terpyridine Iridium(III) Complexes as New Telomerase Inhibitors. *Eur. J. Med. Chem.* **2018**, *143*, 1387–1395. [CrossRef]
41. Ma, Y.; Shen, L.; She, P.; Hou, Y.; Yu, Y.; Zhao, J.; Liu, S.; Zhao, Q. Constructing Multi-Stimuli-Responsive Luminescent Materials through Outer Sphere Electron Transfer in Ion Pairs. *Adv. Opt. Mater.* **2019**, *7*, 1801657. [CrossRef]
42. Heyns, A.M.; van Schalkwyk, G.J. A Study of the Infrared and Raman Spectra of Ammonium Hexafluorophosphate NH_4PF_6 over a Wide Range of Temperatures. *Spectrochim. Acta Part Mol. Spectrosc.* **1973**, *29*, 1163–1175. [CrossRef]
43. Groom, C.R.; Bruno, I.J.; Lightfoot, M.P.; Ward, S.C. The Cambridge Structural Database. *Acta Crystallogr. Sect. B Struct. Sci. Cryst. Eng. Mater.* **2016**, *72*, 171–179. [CrossRef]
44. Frisch, M.J.; Trucks, G.W.; Schlegel, H.B.; Scuseria, G.E.; Robb, M.A.; Cheeseman, J.R.; Scalmani, G.; Barone, V.; Petersson, G.A.; Nakatsuji, H.; et al. Gaussian 16 Rev. C.01 2016. Available online: https://gaussian.com/gaussian16/ (accessed on 1 June 2024).
45. Andrae, D.; Häußermann, U.; Dolg, M.; Stoll, H.; Preuß, H. Energy-Adjustedab Initio Pseudopotentials for the Second and Third Row Transition Elements. *Theor. Chim. Acta* **1990**, *77*, 123–141. [CrossRef]
46. Tang, K.-C.; Liu, K.L.; Chen, I.-C. Rapid Intersystem Crossing in Highly Phosphorescent Iridium Complexes. *Chem. Phys. Lett.* **2004**, *386*, 437–441. [CrossRef]
47. Yoshikawa, N.; Yamabe, S.; Kanehisa, N.; Inoue, T.; Takashima, H.; Tsukahara, K. Detailed Description of the Metal-to-Ligand Charge-Transfer State in Monoterpyridine IrIII Complexes. *Eur. J. Inorg. Chem.* **2009**, *2009*, 2067–2073. [CrossRef]
48. Kuang, Z.; Wang, X.; Wang, Z.; He, G.; Guo, Q.; He, L.; Xia, A. Phosphorescent Cationic Iridium(III) Complexes with 1,3,4-Oxadiazole Cyclometalating Ligands: Solvent-Dependent Excited-State Dynamics. *Chin. J. Chem. Phys.* **2017**, *30*, 259–267. [CrossRef]
49. Lo, K.K.-W.; Chung, C.-K.; Ng, D.C.-M.; Zhu, N. Syntheses, Characterisation and Photophysical Studies of Novel Biological Labelling Reagents Derived from Luminescent Iridium(III) Terpyridine Complexes. *New J. Chem.* **2002**, *26*, 81–88. [CrossRef]
50. Ito, W.; Hattori, S.; Kondo, M.; Sakagami, H.; Kobayashi, O.; Ishimoto, T.; Shinozaki, K. Dual Emission from an Iridium(III) Complex/Counter Anion Ion Pair. *Dalton Trans.* **2021**, *50*, 1887–1894. [CrossRef] [PubMed]
51. Collin, J.-P.; Dixon, I.M.; Sauvage, J.-P.; Williams, J.A.G.; Barigelletti, F.; Flamigni, L. Synthesis and Photophysical Properties of Iridium(III) Bisterpyridine and Its Homologues: A Family of Complexes with a Long-Lived Excited State. *J. Am. Chem. Soc.* **1999**, *121*, 5009–5016. [CrossRef]
52. Arm, K.J.; Leslie, W.; Williams, J.A.G. Synthesis and pH-Sensitive Luminescence of Bis-Terpyridyl Iridium(III) Complexes Incorporating Pendent Pyridyl Groups. *Inorganica Chim. Acta* **2006**, *359*, 1222–1232. [CrossRef]
53. Otaif, H.Y.; Adams, S.J.; Horton, P.N.; Coles, S.J.; Beames, J.M.; Pope, S.J.A. Bis-Cyclometalated Iridium(III) Complexes with Terpyridine Analogues: Syntheses, Structures, Spectroscopy and Computational Studies. *RSC Adv.* **2021**, *11*, 39718–39727. [CrossRef] [PubMed]
54. Ricciardi, L.; Mastropietro, T.F.; Ghedini, M.; La Deda, M.; Szerb, E.I. Ionic-Pair Effect on the Phosphorescence of Ionic Iridium(III) Complexes. *J. Organomet. Chem.* **2014**, *772–773*, 307–313. [CrossRef]
55. Guo, S.; Huang, T.; Liu, S.; Zhang, K.Y.; Yang, H.; Han, J.; Zhao, Q.; Huang, W. Luminescent Ion Pairs with Tunable Emission Colors for Light-Emitting Devices and Electrochromic Switches. *Chem. Sci.* **2016**, *8*, 348–360. [CrossRef] [PubMed]
56. Ilic, S.; Cairnie, D.R.; Bridgewater, C.M.; Morris, A.J. Investigation into Dual Emission of a Cyclometalated Iridium Complex: The Role of Ion-Pairing. *J. Photochem. Photobiol.* **2021**, *8*, 100084. [CrossRef]
57. Earley, J.; Zieleniewska, A.; Ripberger, H.; Lazorski, M.; Mast, Z.; Sayre, H.; Knowles, R.; McCusker, J.; Scholes, G.; Reid, O.; et al. Dipole Moment and Charge Reorganization in Photoredox Catalysts. *ChemRxiv* 2021. [CrossRef]
58. Leslie, W.; Batsanov, A.S.; Howard, J.A.K.; Williams, J.A.G. Cross-Couplings in the Elaboration of Luminescent Bis-Terpyridyl Iridium Complexes: The Effect of Extended or Inhibited Conjugation on Emission. *Dalton Trans.* **2004**, *2004*, 623–631. [CrossRef]
59. Leslie, W.; Poole, R.A.; Murray, P.R.; Yellowlees, L.J.; Beeby, A.; Williams, J.A.G. Near Infra-Red Luminescence from Bis-Terpyridyl Iridium(III) Complexes Incorporating Electron-Rich Pendants. *Polyhedron* **2004**, *23*, 2769–2777. [CrossRef]
60. Flamigni, L.; Ventura, B.; Barigelletti, F.; Baranoff, E.; Collin, J.-P.; Sauvage, J.-P. Luminescent Iridium(III)-Terpyridine Complexes—Interplay of Ligand Centred and Charge Transfer States. *Eur. J. Inorg. Chem.* **2005**, *2005*, 1312–1318. [CrossRef]
61. Goldstein, D.C.; Cheng, Y.Y.; Schmidt, T.W.; Bhadbhade, M.; Thordarson, P. Photophysical Properties of a New Series of Water Soluble Iridium Bisterpyridine Complexes Functionalised at the 4′ Position. *Dalton Trans.* **2011**, *40*, 2053–2061. [CrossRef]

62. Xiang, H.; Cheng, J.; Ma, X.; Zhou, X.; Chruma, J.J. Near-Infrared Phosphorescence: Materials and Applications. *Chem. Soc. Rev.* **2013**, *42*, 6128–6185. [CrossRef] [PubMed]
63. Zhang, Y.; Qiao, J. Near-Infrared Emitting Iridium Complexes: Molecular Design, Photophysical Properties, and Related Applications. *iScience* **2021**, *24*, 102858. [CrossRef] [PubMed]
64. Chelushkin, P.S.; Shakirova, J.R.; Kritchenkov, I.S.; Baigildin, V.A.; Tunik, S.P. Phosphorescent NIR Emitters for Biomedicine: Applications, Advances and Challenges. *Dalton Trans.* **2022**, *51*, 1257–1280. [CrossRef] [PubMed]
65. Liu, B.; Lystrom, L.; Brown, S.L.; Hobbie, E.K.; Kilina, S.; Sun, W. Impact of Benzannulation Site at the Diimine (N^N) Ligand on the Excited-State Properties and Reverse Saturable Absorption of Biscyclometalated Iridium(III) Complexes. *Inorg. Chem.* **2019**, *58*, 5483–5493. [CrossRef] [PubMed]
66. Lu, T.; Lu, C.; Cui, P.; Kilina, S.; Sun, W. Impacts of Extending the π-Conjugation of the 2,2′-Biquinoline Ligand on the Photophysics and Reverse Saturable Absorption of Heteroleptic Cationic Iridium(III) Complexes. *J. Mater. Chem. C* **2021**, *9*, 15932–15941. [CrossRef]
67. Lu, J.; Pan, Q.; Zhu, S.; Liu, R.; Zhu, H. Ligand-Mediated Photophysics Adjustability in Bis-Tridentate Ir(III) Complexes and Their Application in Efficient Optical Limiting Materials. *Inorg. Chem.* **2021**, *60*, 12835–12846. [CrossRef] [PubMed]
68. Li, G.; Jiang, Z.; Tang, M.; Jiang, X.; Tu, H.; Zhu, S.; Liu, R.; Zhu, H. Synthesis, Photophysics and Tunable Reverse Saturable Absorption of Bis-Tridentate Iridium(III) Complexes via Modification on Diimine Ligand. *Molecules* **2023**, *28*, 566. [CrossRef] [PubMed]
69. Han, X.; Wu, L.-Z.; Si, G.; Pan, J.; Yang, Q.-Z.; Zhang, L.-P.; Tung, C.-H. Switching between Ligand-to-Ligand Charge-Transfer, Intraligand Charge-Transfer, and Metal-to-Ligand Charge-Transfer Excited States in Platinum(II) Terpyridyl Acetylide Complexes Induced by pH Change and Metal Ions. *Chem. Eur. J.* **2007**, *13*, 1231–1239. [CrossRef] [PubMed]
70. Choroba, K.; Kotowicz, S.; Maroń, A.; Świtlicka, A.; Szłapa-Kula, A.; Siwy, M.; Grzelak, J.; Sulowska, K.; Maćkowski, S.; Schab-Balcerzak, E.; et al. Ground- and Excited-State Properties of Re(I) Carbonyl Complexes—Effect of Triimine Ligand Core and Appended Heteroaromatic Groups. *Dyes Pigment.* **2021**, *192*, 109472. [CrossRef]
71. Palion-Gazda, J.; Machura, B.; Klemens, T.; Szlapa-Kula, A.; Krompiec, S.; Siwy, M.; Janeczek, H.; Schab-Balcerzak, E.; Grzelak, J.; Maćkowski, S. Structure-Dependent and Environment-Responsive Optical Properties of the Trisheterocyclic Systems with Electron Donating Amino Groups. *Dyes Pigment.* **2019**, *166*, 283–300. [CrossRef]
72. Perdew, J.P.; Burke, K.; Ernzerhof, M. Generalized Gradient Approximation Made Simple. *Phys. Rev. Lett.* **1996**, *77*, 3865–3868. [CrossRef] [PubMed]
73. Adamo, C.; Barone, V. Toward Reliable Density Functional Methods without Adjustable Parameters: The PBE0 Model. *J. Chem. Phys.* **1999**, *110*, 6158–6170. [CrossRef]
74. Ernzerhof, M.; Scuseria, G.E. Assessment of the Perdew–Burke–Ernzerhof Exchange-Correlation Functional. *J. Chem. Phys.* **1999**, *110*, 5029–5036. [CrossRef]
75. Martin, J.M.L.; Sundermann, A. Correlation Consistent Valence Basis Sets for Use with the Stuttgart–Dresden–Bonn Relativistic Effective Core Potentials: The Atoms Ga–Kr and In–Xe. *J. Chem. Phys.* **2001**, *114*, 3408–3420. [CrossRef]
76. Pritchard, B.P.; Altarawy, D.; Didier, B.; Gibson, T.D.; Windus, T.L. New Basis Set Exchange: An Open, Up-to-Date Resource for the Molecular Sciences Community. *J. Chem. Inf. Model.* **2019**, *59*, 4814–4820. [CrossRef] [PubMed]
77. Weigend, F.; Ahlrichs, R. Balanced Basis Sets of Split Valence, Triple Zeta Valence and Quadruple Zeta Valence Quality for H to Rn: Design and Assessment of Accuracy. *Phys. Chem. Chem. Phys.* **2005**, *7*, 3297–3305. [CrossRef]
78. CrysAlis PRO 2011. Available online: https://rigaku.com/ja/products/crystallography/x-ray-diffraction/crysalispro (accessed on 1 June 2024).
79. Sheldrick, G.M. Crystal Structure Refinement with SHELXL. *Acta Crystallogr. Sect. C Struct. Chem.* **2015**, *71*, 3–8. [CrossRef] [PubMed]
80. Szlapa-Kula, A.; Małecka, M.; Maroń, A.M.; Janeczek, H.; Siwy, M.; Schab-Balcerzak, E.; Szalkowski, M.; Maćkowski, S.; Pedzinski, T.; Erfurt, K.; et al. In-Depth Studies of Ground- and Excited-State Properties of Re(I) Carbonyl Complexes Bearing 2,2′:6′,2″-Terpyridine and 2,6-Bis(Pyrazin-2-Yl)Pyridine Coupled with π-Conjugated Aryl Chromophores. *Inorg. Chem.* **2021**, *60*, 18726–18738. [CrossRef]
81. Małecka, M.; Szlapa-Kula, A.; Maroń, A.M.; Ledwon, P.; Siwy, M.; Schab-Balcerzak, E.; Sulowska, K.; Maćkowski, S.; Erfurt, K.; Machura, B. Impact of the Anthryl Linking Mode on the Photophysics and Excited-State Dynamics of Re(I) Complexes [ReCl(CO)3(4′-An-Terpy-κ2N)]. *Inorg. Chem.* **2022**, *61*, 15070–15084. [CrossRef]
82. van Wilderen, L.J.G.W.; Lincoln, C.N.; van Thor, J.J. Modelling Multi-Pulse Population Dynamics from Ultrafast Spectroscopy. *PLoS ONE* **2011**, *6*, e17373. [CrossRef]

Disclaimer/Publisher's Note: The statements, opinions and data contained in all publications are solely those of the individual author(s) and contributor(s) and not of MDPI and/or the editor(s). MDPI and/or the editor(s) disclaim responsibility for any injury to people or property resulting from any ideas, methods, instructions or products referred to in the content.